C O M M U N I C A T I O N S

This Journal is published two issues in a year by the Faculty of Sciences, University of Ankara. Articles and any other material published in this journal represent the opinions of the author(s) and should not be construed to reflect the opinions of the Editor(s) and the Publisher(s).

Research Articles

EVALUATION OF THE IMPACT OF I/Q IMBALANCE COMPENSATION ON COMMUNICATION PERFORMANCE

Gizem Eda SAĞIR[1] and Selçuk TAŞCIOĞLU[1]

[1]Department of Electrical and Electronics Engineering,
Ankara University, Ankara, TURKEY

ABSTRACT. Quadrature mixing is widely used in wireless communication receivers since it provides a solution for image signal problem with low-cost implementations. Image signal is caused by phase and amplitude mismatches between in-phase (I) and quadrature (Q) paths of the receiver. This problem is known as I/Q imbalance and degrades the communication performance if not compensated. In this study, the impact of I/Q imbalance compensation on wireless communication performance is evaluated through experiments and simulations. Simulation results demonstrate that significant communication performance improvement can be achieved in terms of bit error rate (BER) and symbol error rate (SER) by compensating the I/Q imbalance properly. In the experiments, compensation is applied to the signals captured using a software defined radio with zero-IF architecture. Experimental results demonstrate that wireless transmission success rate for the zero-IF receiver is increased by compensating I/Q imbalance.

1. INTRODUCTION

Developments in communication and network technologies, especially with the studies carried out within the framework of 5G and the internet of things (IoT), have increased the widespread use of wireless networks. The growing use of wireless systems increases the demand for low-cost communication receivers. With this demand, architectures compatible with integrated circuits such as zero-IF (zero intermediate frequency) and low-IF (low intermediate frequency) receivers gain importance. These architectures have been developed to provide low-cost solutions for image signal problem which reduces communication performance in receivers.

The main principle of rejecting the image signals in these receivers is to use quadrature mixing, also known as complex mixing [1]. For an ideal quadrature mixer, the image rejection ratio is infinite. However, this ratio is limited in practical systems due to imperfections in the mixers, which causes phase and amplitude imbalances between I and Q paths in the quadrature receiver. This problem leads to interference in both zero-IF and low-IF receivers, therefore increases the bit error rate. Without increasing the cost and complexity of the receiver, digital signal processing algorithms are employed to mitigate the effects of I/Q imbalance. Several techniques have been developed for this purpose. For example, I/Q imbalance compensation was performed digitally for low-IF [2] and zero-IF [3] receivers in order to simplify the analog front-end of the receiver.

Compensation methods for I/Q imbalance can be classified as blind and data-aided. In data-aided methods, compensation is carried out by using prior information of the transmission signals such as training symbols, whereas prior information is not required in blind methods. In most of the wireless communication protocols, training signals are used for synchronization and channel estimation tasks. These known signals have been employed to compensate the mismatches between I and Q channels in data-aided methods [4]. For example, a low complex compensation method was proposed for OFDM based wireless local area network (WLAN) signals in [5]. In this method, legacy long training field (L-LTF) of the WLAN preamble is used for compensation. Performance of the method has been evaluated for different modulation schemes used in IEEE 802.11a/g under AWGN and fading channel conditions. Data-aided methods can have high performance for I/Q imbalance compensation, however these methods require decoding of the transmitted signals. When I/Q imbalance level is high and detection performance is low accordingly, the success of these methods may be limited.

The blind methods are independent of the communication protocol since prior knowledge is not required. This allows these methods to be used in a heterogeneous network including different communication protocols. However, the converge of blind techniques may take a long time in some applications [6]. A blind approach is based on removing the correlation between I and Q signals. Correlation originated from I/Q imbalance makes the complex signals non-proper [7], even if the received communication signal has the properness condition which is a statistical property of quadrature signals. In this approach, the main principle is to make the observed signal proper again by using adaptive filtering, which mitigates the distortion effect of the I/Q imbalance [8]. Another blind technique using adaptive filtering is called interference cancellation. In this technique the image signal is modeled as an interference and estimated using an adaptive filter [8, 9]. In order to obtain an estimation for the desired signal, the estimated interference signal is subtracted from the imbalanced received signal. For the filter adaptation, least mean square (LMS)

or recursive least squares (RLS) approaches can be employed [10]. In [8], this adaptive filtering approach has been performed for the case in which complex conjugate form of the observed signal is taken as reference signal for the filter.

In [11], along with the properness condition for communication signals, a second statistical property called equi-absolute variance condition is used for blind I/Q compensation. The authors have proposed two adaptive compensation methods based on RLS and LMS algorithms. It has been shown by simulations that the proposed method converges to the ideal solution. In [12], statistical characteristics resulted from the modulation and orthogonality of imbalanced quadrature signals for an OFDM system are used for I/Q imbalance compensation.

In this work, the impact of I/Q imbalance and its compensation on wireless communication performance in zero-IF receivers is investigated through simulations and experiments. In the simulations, performance of the method has been evaluated in terms of BER and SER curves. Experimental results have been obtained using a software defined radio. Both simulation and experimental results demonstrate that wireless transmission performance can be enhanced by compensating I/Q imbalance in zero-IF receivers.

2. I/Q Imbalance In Zero-If Receivers

In quadrature downconversion based receivers, gain values in I and Q channels are not equal due to imperfections of the components in analog front-end [7]. This phenomenon is called gain imbalance. Moreover, local oscillator signals generated for I and Q branches do not have ideal phase difference of 90°, which results in phase imbalance. I/Q imbalance is introduced to represent the overall of these distorting effects, which causes image signal problem in the downconversion process. The image signal distorts the desired signal and deteriorates the performance both in transmitter and receiver sides [7, 10].

In zero-IF receiver architecture, the local oscillator signal is generated such that its frequency is equal to the center of the desired RF spectrum in order to downconvert the desired RF signal to the baseband. In this case, negative frequency components of the desired signal occur as the image signal, which is called self-image.

Figure 1 visualizes the downconversion process with a quadrature mixer in the amplitude spectrum. When I/Q imbalance is not present (Fig. 1 left), which is called ideal case, the desired signal is mixed with an exponential at $-f_c$ whose spectrum is represented by blue impulse. In this case, the image problem does not occur since only the desired spectrum is downconverted to the baseband. When I/Q imbalance is present (Fig. 1 right), an unwanted complex exponential occurs at f_c whose spectrum is represented by red impulse. This exponential also downconverts the self-

image signal depicted at $-f_c$. Self-image signal downconverted to the baseband is indicated by dashed red lines. Note that the resulting baseband spectrum is corrupted by the self-image signal and the amount of distortion depends on I/Q imbalance level. As the I/Q imbalance level increases, amplitude of the complex exponential at f_c also increases, which makes the image signal stronger.
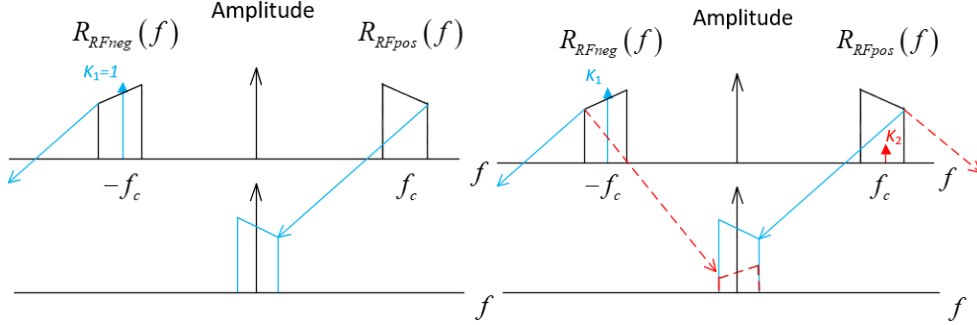
FIGURE 1. Downconversion in zero-IF receivers using quadrature mixer in the ideal case (left) and in the case of presence of I/Q imbalance (right).

Image rejection ratio is theoretically infinite, however due to imperfections of the analog components in the receivers, this ratio is 20-40 dB in practical implementations [9]. High image attenuation level is required especially for high order modulation schemes. Therefore, the distortions caused by image problem should be removed in order to obtain high communication performance in zero-IF receivers, especially for high data rate communication applications.

2.1. **Signal Model.** In zero-IF receiver architecture, quadrature mixing is used to directly downconvert the RF signal to the baseband as shown in Fig. 2. The baseband signal is then low pass filtered and digitized in I and Q branches.
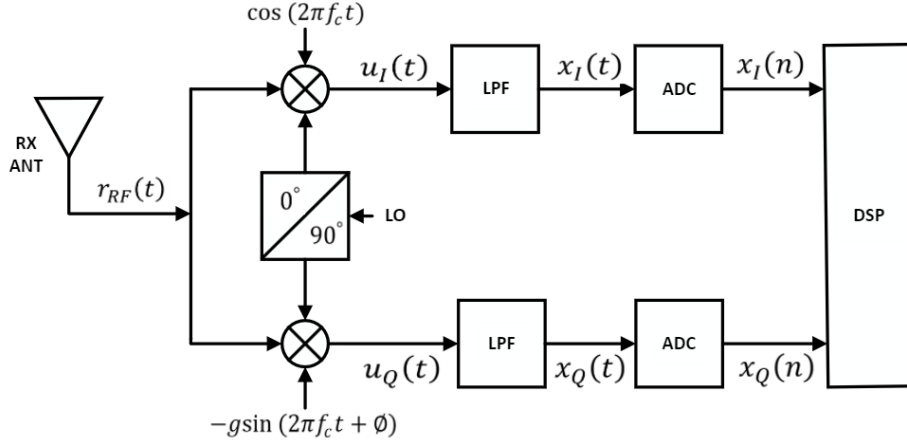
FIGURE 2. Quadrature mixing for zero-IF receivers with I/Q imbalance.

When I/Q imbalance is occurred, the local oscillator (LO) signal which is set to carrier frequency f_c can be modeled as [9]

$$a(t) = \cos(2\pi f_c t) - jg \sin(2\pi f_c t + \emptyset) \tag{1}$$

where $\emptyset$ is phase imbalance and g is gain imbalance (Fig. 2). LO signal can be rewritten by using Euler's equations as

$$a(t) = K_1 e^{-j\omega_c t} + K_2 e^{j\omega_c t} \tag{2}$$

where $K_1 = \frac{1+ge^{-j\emptyset}}{2}, K_2 = \frac{1-ge^{j\emptyset}}{2}$. The degree of I/Q imbalance can be quantified by defining the image rejection ratio (IRR) as follows [11]

$$IRR = 10log_{10} \frac{|K_1|^2}{|K_2|^2} \tag{3}$$

In the ideal case $g = 1$ and $\emptyset = 0,$ and therefore $K_1 = 1$ and $K_2 = 0$, which results in infinite IRR.

The received RF signal can be represented as

$$r_{RF}(t) = r_{RFpos}(t) + r_{RFneg}(t) \tag{4}$$

where $r_{RFpos}(t)$ and $r_{RFneg}(t)$ represent time domain signals corresponding to the positive and negative frequency components, namely $R_{RFpos}(f)$ and $R_{RFneg}(f)$, of RF signal shown in Fig. 1. By multiplying LO signal in (2) with RF signal in (4), the signal at the mixer's output is obtained as follows

$$u(t) = K_1 e^{-j\omega_c t} r_{RFpos}(t) + K_2 e^{j\omega_c t} r_{RFneg}(t) +$$

$$\underbrace{K_2 e^{j\omega_c t} r_{RFpos}(t) + K_1 e^{-j\omega_c t} r_{RFneg}(t)}_{high\ frequency\ terms} \qquad (5)$$

After filtering high frequency terms in (5) using a low pass filter, the baseband I/Q imbalanced analog signal model is given as [13]

$$x(t) = K_1 e^{-j\omega_c t} r_{RFpos}(t) + K_2 e^{j\omega_c t} r_{RFneg}(t) \qquad (6)$$

$x(t)$ can also be expressed as

$$x(t) = K_1 r(t) + K_2 r^*(t) \qquad (7)$$

where $r(t)$ and $r^*(t)$ denote the ideal analog baseband signals when there is no I/Q imbalance and are defined as

$$r(t) = e^{-j\omega_c t} r_{RFpos}(t) \qquad (8)$$

$$r^*(t) = e^{j\omega_c t} r_{RFneg}(t) \qquad (9)$$

Note that these ideal baseband signals can only be obtained in the case that I/Q imbalance is not present, in which case $x(t) = r(t)$ since $K_1 = 1$ and $K_2 = 0$.

The digitized version of the imbalanced received baseband signal in (7) is defined as

$$x(n) = K_1 r(n) + K_2 r^*(n) \qquad (10)$$

where n denotes the discrete time index.

3. I/Q Imbalance Compensation

Distortions due to I/Q imbalance increases as the level of receiver hardware imperfections increases. This may degrade the communication performance

significantly. The effect of interference caused by the image signal in zero-IF receivers can be mitigated by compensating the I/Q imbalance. Statistical features of the signals or known characteristics of the transmitted signals can be employed for this purpose. Blind and data-aided approaches used in this paper are presented in the following subsections.

3.1. **Adaptive Filtering Based Blind I/Q Imbalance Compensation.** I/Q imbalance compensation can be performed by subtracting estimated interference signal from the observed imbalanced signal $x(n)$. This approach is known as interference cancellation. Interference signal can be estimated by using an adaptive filter [9], [10] as shown in Figure 3. In this approach the main issue is defining a reference signal $v(n)$ applied to adaptive filter. Adaptive filter coefficients $w(n)$ can be calculated by using LMS or RLS algorithms [10].
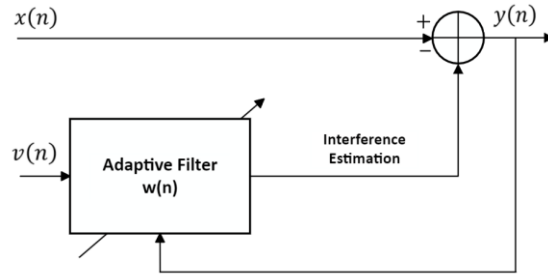
FIGURE 3. Interference cancellation approach using adaptive filtering [9].

In blind I/Q imbalance compensation methods, statistical properties of the signal can be employed. One of these statistical properties is the properness which is satisfied for many communications signals [14]. The distortions caused by wireless channels do not affect the properness condition for communications signals [15]. On the other hand, I/Q imbalance leads to improper signals at the receiver even if the transmitted signal is proper [14]. Considering these facts, compensation techniques based on ensuring that the received signal has the properness condition again have been proposed [8, 11]. For this purpose, adaptive filtering is employed in [8]. In this method, the reference signal for adaptive filter is taken as the complex conjugate of the I/Q imbalanced signal such that $v(n) = x^*(n)$. By using LMS algorithm filter adaptation is carrier out as follows [8]

$$y(n) = x(n) + w^T(n)x^*(n) \tag{11}$$
$$w(n+1) = w(n) - \mu y(n)y(n) \tag{12}$$

where $x(n)$ is I/Q imbalanced signal and $y(n)$ is compensated signal. The filter coefficients are represented by $w(n)$ and μ denotes step size. The step size should be determined by considering the characteristics of the application. An optimization approach for determining the step size for this method is proposed in [16].

In [11], a second statistical property called equi-absolute variance condition in addition to properness condition for communication signals is employed to compensate the I/Q imbalance. The compensated baseband signal $y(n) = y_I(n) + jy_Q(n)$ is obtained as follows [11]

$$y_I(n) = x_I(n) \tag{13}$$
$$y_Q(n) = \hat{\beta}\left(\hat{\alpha}x_I(n) + x_Q(n)\right) \tag{14}$$

where $x_I(n)$ and $x_Q(n)$ are defined as the I and Q components of the received imbalanced baseband signal which is given in the form of $x(n) = x_I(n) + jx_Q(n)$. $\hat{\alpha}$ and $\hat{\beta}$ denote the estimated compensation parameters which include gain and phase imbalances. In order to estimate these parameters, two different adaptive filtering approaches based on RLS and LMS algorithms were proposed in [11].

3.2. **Data-Aided Compensation Method for OFDM based WLAN.** WLAN signals contain known training signals and pilots for synchronization and channel estimation tasks. This prior information about the transmitted signals can be employed to compensate the I/Q imbalance. In [5], a low complex I/Q imbalance compensation method using legacy long training field (L-LTF) of the WLAN preamble was proposed for OFDM based WLAN systems. In this method, for a complex valued I/Q imbalanced L-LTF signal $z(n) = z_I(n) + jz_Q(n)$, I/Q imbalance correction factors are calculated as

$$\rho = \sqrt{\frac{\sum_n^L z_Q^2(n)}{\sum_n^L z_I^2(n)}} \tag{15}$$

$$\zeta = \frac{\sum_n^L(z_I(n)z_Q(n))}{\sum_n^L z_I^2(n)} \tag{16}$$

where L is the length of one OFDM symbol without cyclic prefix in L-LTF signal. I and Q components of the compensated signal is obtained as follows

$$y_I(n) = \frac{x_I(n)}{\rho} \tag{17}$$

$$y_Q(n) = \frac{1}{\sqrt{1-\zeta^2}}\left[x_Q(n) - \zeta x_I(n)\right] \tag{18}$$

4. RESULTS

4.1. **Simulation Results.** The impact of I/Q imbalance and its compensation on the constellation diagram is visualized for 16 QAM symbols in Fig. 4. Blue circles indicate the symbols corrupted by additive white Gaussian noise such that SNR is 25 dB for the case that there is no I/Q imbalance. Red circles show the symbols observed when there is I/Q imbalance with $g = 1.2$ and $\emptyset = 10°$. When the I/Q imbalance is compensated, improved constellation diagram is represented with yellow circles. Note that the compensation mitigates the distortions due to I/Q imbalance and makes the symbols close to the reference ideal symbols observed in the absence of I/Q imbalance.
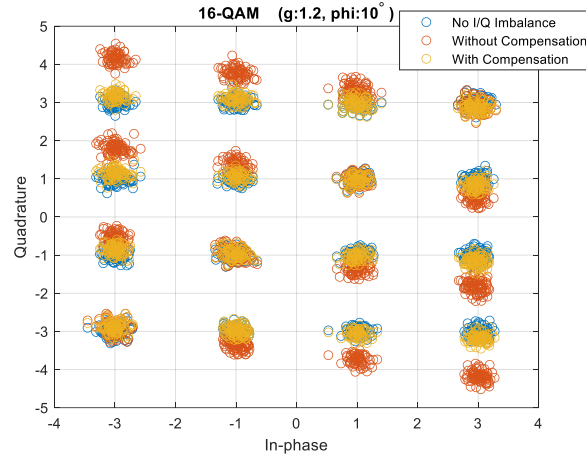
FIGURE 4. Constellation diagram for 16 QAM: No I/Q imbalance (blue), with I/Q imbalance (red), compensated (yellow).

Monte Carlo simulations were performed to evaluate the impact of I/Q imbalance compensation on wireless communication performance in terms of SER and BER curves. Three blind and a data-aided compensation methods were applied to the distorted signals with the same amplitude and phase imbalance values for a fair comparison. BER and SER performance for I/Q imbalanced and compensated cases by using different methods were evaluated for different SNR levels. In each SNR level, BER and SER values are calculated from the randomly generated data consisting of 100.000 bits. Average error rates are calculated over 100 Monte Carlo simulations with different realizations of additive white Gaussian noise.

In order to determine the imbalance values, four different cases in which gain and phase imbalances take different values were considered. Performance degradation for different imbalance values is given in terms of BER versus SNR in Fig. 5. This

figure shows that BER performance degrades as the phase and gain imbalance values increase. For the simulations performed to observe the compensation effect, phase imbalance is set to 10° and gain imbalance is set to 1.2. For these imbalance values, image rejection ratio is found to be approximately 18 dB by using (3). This is close to the image rejection ratio encountered in practical implementations [9].
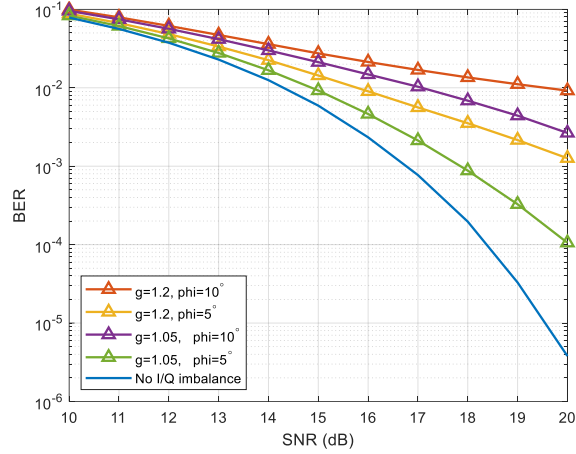
FIGURE 5. BER versus SNR curves for 16 QAM in the ideal case (no IQ imbalance) and in the cases where signals are distorted with different I/Q imbalance values.

The impact of I/Q imbalance compensation for two different modulation level of 16 and 64 QAM was evaluated. BER and SER curves are given in Fig. 6 for four different compensation methods. Note that BER and SER performances are lower for 64 QAM compared to those obtained for 16 QAM. The underlying reason is that as the QAM level increases, the distances between symbols get smaller, resulting in higher error rates. Therefore, I/Q imbalance compensation becomes more crucial when the level of QAM is high. These figures show that BER and SER performances significantly increase with I/Q imbalance compensation for both QAM levels. The performances of the data-aided [5] and RLS based blind adaptive [11] compensation methods are very close to the ideal performance that is obtained when there is no I/Q imbalance. Note that RLS based blind adaptive [11] compensation method achieves this performance without any prior information. Similar performances were obtained with complex conjugate [8] and LMS based [11] blind adaptive compensation methods. Performances of these methods are slightly lower than that of the ideal case as the SNR level increases.
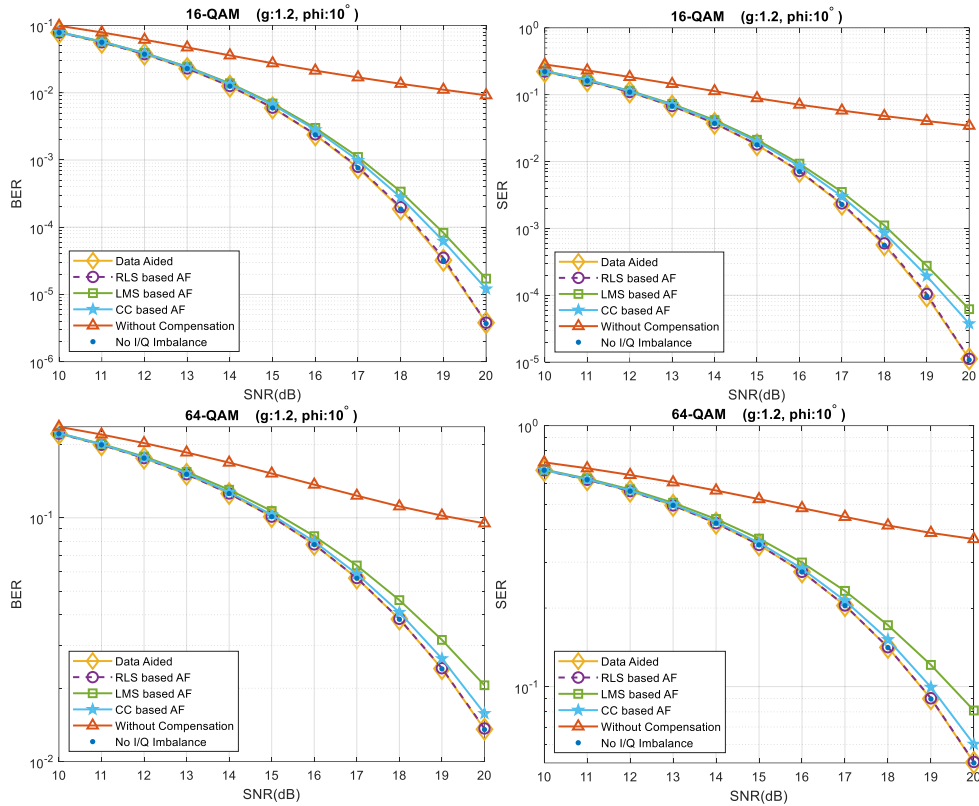
FIGURE 6. BER and SER performance improvement with I/Q imbalance compensation by using data-aided and adaptive filtering (AF) based methods for different SNR values.

4.2. **Experimental Results.** The performance improvement through I/Q imbalance compensation for a wireless communication system using software defined radio (SDR) was evaluated by experiments. The experimental setup consisting of a computer with MATLAB software and a SDR with zero-IF architecture is given in Fig. 7. The computer and SDR are connected with a USB cable. In the experiments, an image is transmitted through a wireless channel by using SDR. OFDM based data packets consisting of 64 QAM symbols are generated based on IEEE 802.11g protocol by using WLAN toolbox in MATLAB and transmitted over a wireless network [17]. The center frequencies of the transmitter and receiver were set to 2.427 GHz. At the receiver side of SDR, signals were downconverted to the baseband located at [-10, 10] MHz and digitized at a sampling rate of 30 MSamples/s. Data packets were decoded using WLAN toolbox after compensating I/Q imbalance with different methods.
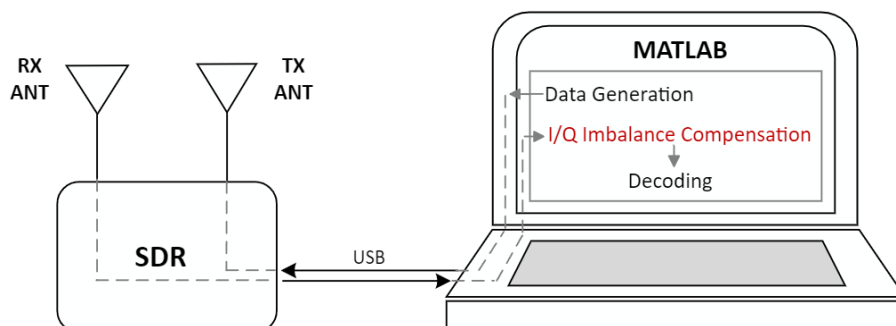
FIGURE 7. Experimental setup.

In the experiments, transmission success ratios were calculated over a hundred tests for the cases in which I/Q imbalance is not compensated and compensated with adaptive filtering (AF) based blind methods. The average results are given in Table 1. The data-aided method implemented in Section 4.1 cannot be used for the experiments since this method requires the preamble part of the WLAN signals, which is inaccessible in this experimental setup. Transmission success ratio was calculated as 55% when I/Q imbalance was not compensated. This ratio was improved about 20-30% via I/Q imbalance compensation using different blind adaptive filtering based methods. It should be noted that the experiments were not performed under ideal conditions. Therefore, the performance results of the methods may change for different experiments due to random nature of wireless channels, e.g. interference and multipath channel distortions. The main result of Table 1 is that all the adaptive filtering (AF) based methods implemented for I/Q imbalance compensation provide a considerable performance improvement in terms of transmission success ratio for the cases in which I/Q imbalance is not compensated and compensated.

TABLE 1. Transmission success ratio calculated over a hundred tests

Methods	Success Ratio (%)
Not compensated	55
RLS based AF	75
LMS based AF	78
Complex Conjugate AF	85

5. Conclusions

I/Q imbalance problem in zero-IF receivers and compensation approaches for this problem are examined. Performance improvement of different compensation techniques have been evaluated by using experimental and simulation data. It has been demonstrated by simulations that the distorting effect due to I/Q imbalance increases as the imbalance values increases. Simulation results also illustrate that SER and BER performances can be improved significantly by compensating the I/Q imbalance. In simulations, the performance of the RLS based adaptive filtering method is very close to that of the data-aided method. This is an important result showing that a performance improvement can be achieved using a blind method as high as obtained with a data-aided method.

Experimental results obtained from an OFDM based WLAN system by using a software defined radio illustrate that a considerable performance improvement via blind I/Q imbalance compensation in terms of transmission success ratio can be achieved for zero-IF architecture. Regarding the fact that protocol independent approaches gain importance for the heterogeneous networks including devices using different protocols, the experimental results showing that blind methods can be employed in these networks with a sufficient performance are considered to be important.

Author Contribution Statements The authors contributed equally to this work.

Declaration of Competing Interests The authors declare that they have no known competing financial interests or personal relationships that could have appeared to influence the work reported in this paper.

References

[1] Lyons, R. G., Understanding Digital Signal Processing, Prentice Hall, 2011.

[2] Windisch, M., Fettweis, G., Blind I/Q imbalance parameter estimation and compensation in low-IF receivers, *First International Symposium on Control, Communication and Signal Processing*, (2004), 75-78, https://doi.org/10.1109/ISCCSP.2004.1296222.

[3] Windisch, M., Fettweis, G., On the performance of standard-independent I/Q imbalance compensation in OFDM direct-conversion receivers, *13th European Signal Processing Conference*, (2005), 1-5.

[4] Windisch, M., Estimation and Compensation of IQ Imbalance in Broadband Communications Receivers, Jörg Vogt Verlag, Germany, 2007.

[5] Held, I., Klein, O., Chen, A., Ma, V., Low complexity digital IQ imbalance correction in OFDM WLAN receivers, *2004 IEEE 59th Vehicular Technology Conference*, *VTC 2004-Spring (IEEE Cat. No.04CH37514)*, 2 (2004), 1172-1176, https://doi.org/10.1109/VETECS.2004.1389017.

[6] Gomaa, A., Jalloul, L. M. A., Data-Aided I/Q imbalance estimation and compensation in OFDM systems, *IEEE Commun. Lett.*, 18 (3) (2014), 459-462, https://doi.org/10.1109/LCOMM.2014.012014.132321.

[7] Hakkarainen, A., I/Q Imbalance in Multiantenna Systems: Modeling, Analysis and RF-Aware Digital Beamforming, *Ph.D. Dissertation, Tampere University of Technology,* Finland, 1447, 2017.

[8] Anttila, L., Valkama, M., Renfors, M., Blind compensation of frequency-selective I/Q imbalances in quadrature radio receivers: Circularity-based approach, *2007 IEEE International Conference on Acoustics, Speech and Signal Processing – ICASSP '07*, (2007), 245-248, https://doi.org/10.1109/ICASSP.2007.366518.

[9] Valkama, M., Advanced I/Q Signal Processing for Wideband Receivers: Models and Algorithms, *Ph.D. Dissertation, Tampere University of Technology,* Finland, 2001.

[10] Valkama, M., Renfors, M., Koivunen, V., Advanced methods for I/Q imbalance compensation in communication receivers, *IEEE Trans. Signal Process.*, 49 (10) (2001), 2335-2344, https://doi.org/10.1109/78.950789.

[11] Nam, W., Roh, H., Lee, J., Kang, I., Blind Adaptive I/Q imbalance compensation algorithms for direct-conversion receivers, *IEEE Signal Process. Lett.*, 19 (8) (2012), 475-478, https://doi.org/10.1109/LSP.2012.2202902.

[12] Xu, Z., Cheng, Y.B., Ren, S.J., Estimation and compensation of I/Q imbalance in millimeter-wave OFDM UWB system, *J. Comput.*, 28 (4) (2017), 179-188, https://doi.org/10.3966/199115592017082804019.

[13] Valkama, M., Renfors, M., Advanced DSP for I/Q imbalance compensation in a low-IF receiver, 2000 IEEE International Conference on Communications, *Global Convergence Through Communications, Conference Record,* 2 (2000), 768-772, https://doi.org/10.1109/ICC.2000.853603.

[14] Adali, T., Schreier, P. J., Scharf, L. L., Complex-valued signal processing: the proper way to deal with impropriety, *IEEE Trans. Signal Process.*, 59 (11) (2011), 5101-5125, https://doi.org/10.1109/TSP.2011.2162954.

[15] Anttila, L., Valkama, M., Renfors M., Circularity-based I/Q imbalance compensation in wideband direct-conversion receivers, *IEEE Trans. Veh. Technol.*, 57 (4) (2008), 2099-2113, https://doi.org/10.1109/TVT.2007.909269.

[16] Petrovic, M., Milic, M., Milenkovic, S., Optimal parameters of the IQ imbalance correction algorithm based on adaptive filter, *Proceedings of 4th International*

Conference on Electrical, Electronics and Computing Engineering IcETRAN 2017, (2017), 1-5.

[17] MathWorks, https://www.mathworks.com/help//supportpkg/plutoradio/ug/transmission-and-reception-of-an-image-using-wlan-system-toolbox-and-a-single-pluto-radio.html, 2022.

UTILIZATION OF DEEP LEARNING ARCHITECTURES FOR MIMO DETECTION

Sümeye Nur KARAHAN[1] and Aykut KALAYCIOĞLU[1]

[1]Department of Electrical and Electronics Engineering,
Ankara University, Ankara, TURKEY

ABSTRACT. Applications of deep learning in communications systems are becoming popular today with their powerful solutions to complex problems. This study considers the utilization of deep learning detectors for small-scale multiple-input multiple-output systems. Deep neural network, long short-term memory, and one-dimenisonal convolutional neural network architectures are discussed and the bit error rate performances of these deep learning based detectors are compared with the optimal maximum likelihood and sub-optimal minimum mean square error detectors. Simulation results show that the deep neural network architecture has the best detection performance among the discussed deep learning detectors and may outperform the sub-optimal minimum mean square error detector. For small-scale multiple-input multiple-output systems, the performance of the deep learning based detector is close to that of the optimal detector.

1. INTRODUCTION

Unlike the single-input single-output (SISO) systems, in a multiple-input multiple-output (MIMO) system, both the transmitter and the receiver employ more than one antennas to transmit and receive signals at the same time. MIMO technique is a promising technology for the current and next generation systems with the aim of enhancing the spectral efficiency and increasing the reliability. To increase the reliability, in a diversity system the transmitter conveys the same information through multiple antennas, while a MIMO system using spatial multiplexing transmits different signals over a group of transmitter antennas to improve the spectral efficiency.

Traditional MIMO detection techniques have been discussed in the literature [1, 2] for many years. Detection complexity and performance are among the biggest concerns in a typical MIMO system. Among these detection techniques, maximum likelihood (ML) detector has the optimum performance in terms of bit error rate. However, the increasing complexity with the number of antennas makes this technique unfeasible for practical systems. On the other hand, the sub-optimal detection techniques such as the minimum mean square error (MMSE), zero forcing (ZF), Gauss-Seidel, and conjugate-gradient (CG) cause a significant performance degradation while reducing the complexity [3-5].

Deep learning (DL) approaches have brought powerful solutions in many areas such as image and speech recognition, computer vision, and wireless communications for more than two decades [6]. In recent years, DL approaches are also considered as an auspicious solution for MIMO signal detection [7, 8]. DL based MIMO detection is mainly based on two different approaches, model-based and data-driven. Model-based approaches simply unfold the iterations of a well-known detection technique as the layers of a deep learning structure [9,10]. The combination of neural networks with an iterative detection method improves the detection performance and decreases the computation complexity. Also, although the model-based structure is mainly based on DL approaches, it can be trained with much less training data than a traditional data-driven DL algorithm.

In the literature, there are many recent studies that discuss model-based and data-driven approaches. For instance, in [11], a model-based deep learning detection technique for MIMO systems is proposed. Authors state that the proposed technique has a better detection performance than the existing sub-optimal detectors and a lower computational complexity. Another model-based deep learning detection technique, which depends on the orthogonal approximate message passing (OAMP) algorithm, for a MIMO system is discussed in [12]. The proposed technique inserts new parameters to the iterative algorithm to improve the detection performance. The simulation results show that the proposed technique has a superior performance than does the iterative OAMP algorithm under different channel conditions. In [3], instead of adding new parameters to an iterative algorithm, the authors proposed to learn a universal step size value using a model-based DL technique based on conjugate gradient detector. The results show that proposed technique may outperform the performance of the iterative CG detector when the number of antennas is high. On the other hand, purely data-driven MIMO detection solutions are also discussed in the literature for a while. One of the first studies for MIMO detection in the literature is discussed in [13] in which an unsupervised deep learning structure for a MIMO system is proposed by using an autoencoder. Authors claim that DL based solution has a remarkable performance for the MIMO system compared to the existing methods. In [14], two deep neural networks are proposed

for MIMO detection and authors state that the proposed DL structures have a high detection accuracy. A recent study [15] discusses DL based MIMO detection for a conventional MIMO system by using deep neural network (DNN) and convolutional neural network (CNN) structures for fixed channel scenarios. The results show that DNN based data-driven structure has a detection performance close to the optimum detection performance for a single-tap channel model, while for multi-tap fixed channel models both CNN and DNN have an acceptable performance at low SNR values. In [16] a DL detection performance for a MIMO system with an erroneous channel information is proposed. Authors state that DNN has a better bit error rate (BER) performance than the CNN structure. Also, authors in [17] discuss a combination of two DNN structures for MIMO detection. They state that the detection performance is close to the optimal maximum likelihood detector. In [18] DL based MIMO detection is studied in an optical transmission system and the results of the proposed structure are compared with traditional detectors.

To sum up, both model-based and data-driven DL based MIMO detection structures have been discussed for the past few years as mentioned above. This study discusses the MIMO detection in terms of various data-driven DL networks such as DNN, long short-term memory (LSTM), and one-dimensional convolutional neural network (1DCNN) architectures. Several MIMO systems with different number of transmitter and receiver antennas are considered to compare the performance of the proposed detectors. Besides, binary phase-shift keying (BPSK), quadrature phase-shift keying (QPSK), and 16-quadrature amplitude modulation (16-QAM) schemes are utilized. Simulation results show that DL based MIMO detectors have a remarkable detection performance and may surpass the detection performance of the sub-optimal detectors.

Organization of this study is as follows. Section 2 describes the system model of the discussion. In Section 3, we will give the details of the proposed structures. Simulation parameters and results are given in Section 4. Finally, a brief conclusion is discussed in Section 5.

2. MIMO SYSTEM MODEL

In this study, we discuss a conventional $N_r \text{x} N_t$ MIMO system, given in Figure 1, using spatial multiplexing on the transmitter side. Thus, multiple symbols, x_{N_t} are transmitted at the same time with the N_t transmitting antennas. The received symbols, y_{N_r} at the N_r receiver antenna can be given as follows:

$$\begin{bmatrix} y_1 \\ y_2 \\ \vdots \\ y_{N_r} \end{bmatrix} = \begin{bmatrix} h_{1,1} & \dots & h_{1,N_t} \\ \vdots & \dots & \vdots \\ h_{N_r,1} & \dots & h_{N_r,N_t} \end{bmatrix} \begin{bmatrix} x_1 \\ x_2 \\ \vdots \\ x_{N_t} \end{bmatrix} + \begin{bmatrix} n_1 \\ n_2 \\ \vdots \\ n_{N_r} \end{bmatrix} \tag{1}$$

where h_{N_r,N_t} is the entries of the channel matrix between the N_t-th transmitter antenna and N_r-th receiver antenna, n_{N_r}-th is the additive white Gaussian noise (AWGN), having zero mean and σ^2 variance, in the N_r-th receiver antenna. x_{N_t}, y_{N_r}, n_{N_r}, and h_{N_r,N_t} are complex-valued numbers and the channel represents a flat Rayleigh fading. The channel entries, h_{N_r,N_t} are assumed to be independent and identically distributed (i.i.d) with zero mean and unit variance.
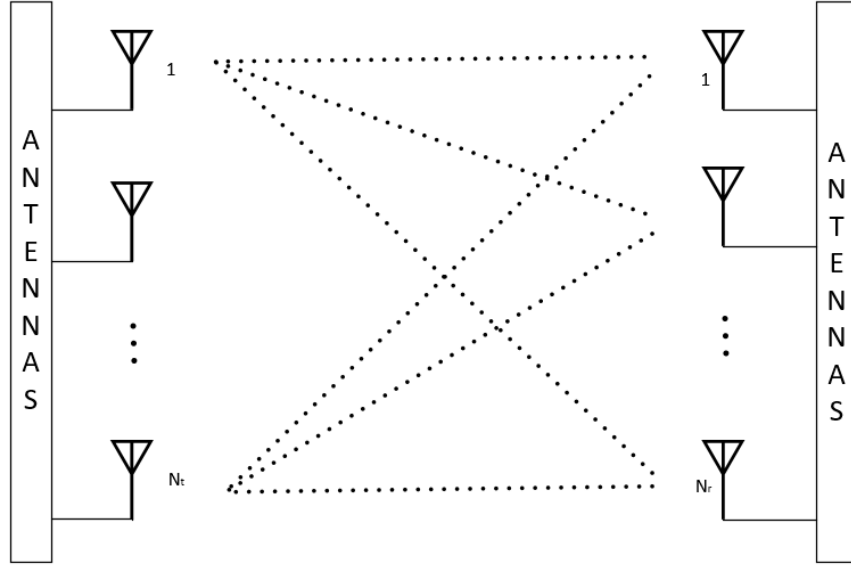
FIGURE 1. Simplified block diagram of a MIMO system.

We discuss two fundamental detection techniques within this section. The optimal maximum likelihood (ML) detector compares all the transmitted symbols and proceeds a likelihood test; therefore, the estimated symbol, $\hat{x}_{ML}$ can be given as follows:

$$\hat{x}_{ML} = \arg min \, \|y - Hx\|^2 \tag{2}$$

where y, H, and x are the received symbol, perfectly known channel matrix, and transmitted symbol, respectively.

Sub-optimal detection methods are also available for conventional MIMO systems. For instance, well-known MMSE detector attempts to minimize the mean square error between the transmitted symbol and the received symbol. The estimated symbol, $\hat{x}_{MMSE}$ can be given as follows:

$$\hat{x}_{MMSE} = W_{MMSE}^H y = (H^H H + \sigma^2 I_{N_T})^{-1} H^H y \qquad (3)$$

where W_{MMSE}^H represents the Gramian matrix and the superscript H denotes the Hermitian transpose operator. Besides, σ^2 and I_{N_T} are the noise variance and the identity matrix, respectively.

Basically, both methods rely on the perfectly known channel matrix, while the MMSE detector has a lower complexity than the ML detector but causes degradation in detection performance in a conventional MIMO system.

3. DATA-DRIVEN DEEP LEARNING ARCHITECTURES FOR MIMO DETECTION

In this section, we will briefly present the utilization of DNN, LSTM, and 1DCNN architectures for MIMO detection. All of these DL architectures employ a supervised learning using a mapping function between the input and output variables.

Typically, a DNN structure, shown in Figure 2, consists of the input layer, a series of hidden layers, and the output layer. The number of hidden layers and the number of hidden units of each layer vary depending on the complexity of the problem and the performance requirements. Hidden layers mainly provide both a linear and nonlinear relation between the input and output of each layer. This dependency consists of a multiplication matrix w, a bias vector b, and a nonlinear activation function, f. Therefore, depending on the previous layer, the n-th layer output, y_n can be given as follows [19]:

$$y_n = f(w_n \cdot y_{n-1} + b_n) \qquad (4)$$

Although different activation functions such as hyperbolic tangent (tanh) or sigmoid can be employed to ensure the nonlinearity of this dependency, nowadays many DNN structure use rectified linear unit (ReLU) activation function, given in (5), which is also a powerful solution for the vanishing gradient problem:

$$ReLU(x) = \begin{cases} x, & x \geq 0 \\ 0, & x < 0 \end{cases} \qquad (5)$$

The output layer of a typical DNN architecture generally employs a softmax function to obtain the predicted output. Adam optimizer is usually employed to minimize the loss function based on cross-entropy.

Hyper parameters also play a crucial role in deep learning algorithms during the training process. Learning rate, batch size, number of epochs, and normalization of data will definitely affect the performance of the network [15].
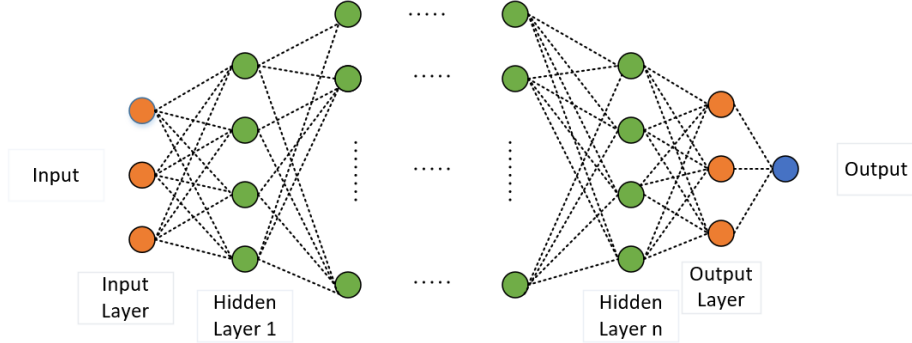
FIGURE 2. Simplified deep neural network (DNN) architecture.

MIMO channel model discussed in (1) is utilized for the DL network. Therefore, the complex-valued system model needs to be converted to an equivalent real domain representation, as shown in (6), to be processed by the deep learning functions. In this equation $Re\{.\}$ and $Im\{.\}$ represents the real and imaginary parts of the complex-valued number, respectively [12, 20]:

$$\begin{bmatrix} Re\{y\} \\ Im\{y\} \end{bmatrix} = \begin{bmatrix} Re\{H\} & -Im\{H\} \\ Im\{H\} & Re\{H\} \end{bmatrix} \begin{bmatrix} Re\{x\} \\ Im\{x\} \end{bmatrix} + \begin{bmatrix} Re\{n\} \\ Im\{n\} \end{bmatrix} \qquad (6)$$

A classification of deep networks can be made by the direction of the data flow from the input layer to the output layer. In a feed-forward neural network (FFFN), input data can only move in the forward direction whereas a feedback loop exists in a recurrent neural network (RNN) [21]. In addition to the discussed DNN structure above, CNN is another subclass of FFFN, while LSTM is a typical example of RNN.

While two-dimensional CNN (2DCNN) architecture is a powerful solution for image processing, in this study for MIMO signal detection, we implement the 1DCNN architecture, which is an influential technique for times series and vector data. In a typical CNN structure, in addition to the fully connected layer a convolutional layer is employed to filter the input data by the linear convolution operation. Besides, a pooling layer, which separates the data into sub-blocks to get the maximum or average of each block, is often utilized in a CNN structure. In 1DCNN architecture, both convolutional filter and pooling layers are employed to the one dimensional inputs. A typical activation function such as ReLU and a fully connected layer are also required to construct the 1DCNN structure.

As an RNN structure, LSTM can also be utilized for problems involving correlated samples or time series [20, 21]. Unlike DNN or CNN as examples of FFFN, LSTM allow both forward and reverse flow of data. In an LSTM network

architecture, an LSTM layer consists of input, forget, and output gates. Depending on these gates, LSTM architecture decides which information will be passed to other layers, whether it is important to remember, and how this information will affect the dependency in the input data. Although LSTM architecture is considered as a suitable solution for time series and correlated samples, it can also be employed in MIMO signal detection [15, 20]. An LSTM architecture basically consists of LSTM layers with different number of hidden units and a fully connected layer.

In general, DL based algorithms require a large amount of training data for the architecture to learn variables and provide high performance, which increase the computational complexity. In addition, number of layers, number of filters, filter sizes, type of activation function also affect both the complexity and the learning performance of the network. However, in many practical deep learning applications, training is an offline process and the computational complexity of learning algorithms is not considered as a major burden for the feasibility of these approaches.

4. SIMULATION PARAMETERS AND RESULTS

In this study, we utilized three different deep learning network architectures of similar complexity, DNN, 1DCNN, and LSTM, to discuss the detection performance of a conventional MIMO system with different modulation levels and number of antennas. Besides, ML and MMSE detectors were implemented to compare the detection performance of the proposed DL based architectures with optimal and sub-optimal detectors, respectively. Main simulation parameters used for DL based detectors are given in Table 1.

TABLE 1. Main simulation parameters.

Parameter	Value
Number of Transmitter Antennas	2, 4
Number of Receiver Antennas	2, 4, 8, 16
Modulation Types	BPSK, QPSK, 16-QAM
Detector Types	ML, MMSE, DNN, LSTM, 1DCNN
Activation Function	ReLU
Mini Batch Size	10000
Maximum Number of Epochs	1000
Optimizer	Adam
Learning Rate	0.001
Number of Training Trials	500,000
Number of Test Trials	100,000

Within this section, we will present the bit error rate performance of the mentioned detectors over several signal-to-noise ratio (SNR) values. In all simulations, we assume that the channel is perfectly known at the receiver for conventional detectors and for DL based detectors the channel matrix is given to the DL input layer along with the received signal. In each trial a new channel was randomly generated and used to transmit the symbols simultaneously. A MIMO simulator in Python was implemented to generate and transmit symbols over a Rayleigh fading channel with additive white Gaussian noise, having different noise variances.

DNN architectures employed five fully connected layers with different number of hidden units to perform the detection of the symbols, while LSTM architecture used three LSTM layers and one fully connected layer. 1DCNN architecture has two one-dimensional convolutional layers and one fully connected layer. In all simulations, number of hidden parameters, filter sizes, and number of filters were set the same regardless of the difficulty of the detection problem. During the training process, ReLU activation function and Adam optimizer were used with a fixed learning rate.

a)   BPSK   b)   QPSK
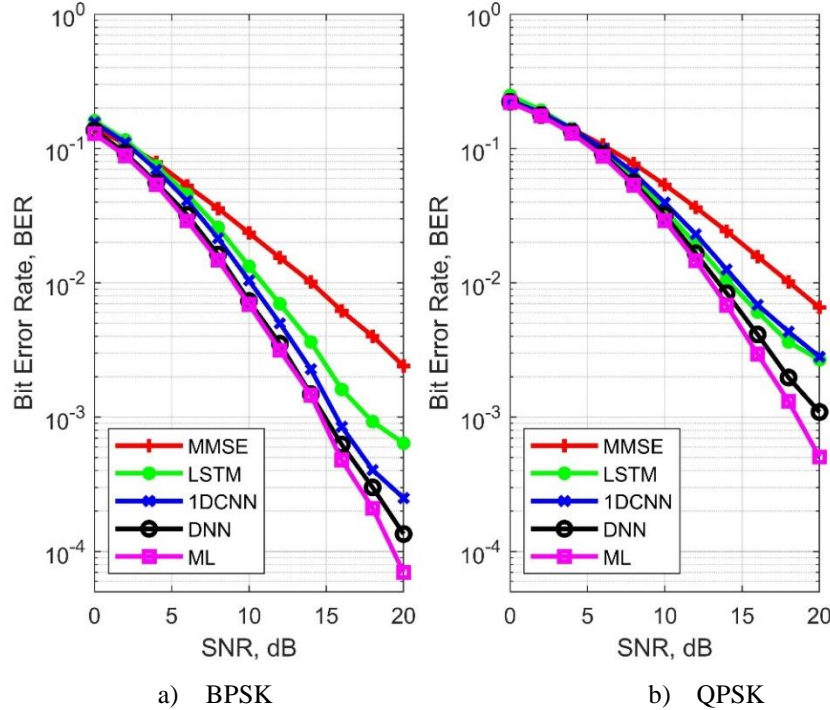
FIGURE 3. Bit error rate performance of detectors over 2x2 MIMO system.

For all DL based detectors, the input consists of the channel matrix and received symbols and is expressed as a one-dimensional vector of real and imaginary parts of these values. Besides, softmax layer and one-hot encoding were employed to perform the classification at the output layer, in which the number of labels depend on the number of modulation order and the number of antennas at the transmitter.

Figure 3 shows the BER performance of the discussed detectors over a 2x2 MIMO system with BPSK and QPSK modulations.

As shown in Figure 3, all three DL based detectors have a high detection performance in terms of bit error rate. Performance of the DNN and 1DCNN is close to that of the optimal ML detector for BPSK modulation, while for QPSK modulation DNN outperforms the 1DCNN detector. In both cases, DL based detectors have a better detection performance than the MMSE detector. Simulation results show that DNN has the best detection performance among these three DL based detectors for both BPSK and QPSK modulation over a 2x2 MIMO system.

In Figure 4, we now compare the detection performance of the mentioned detectors for a 4x4 MIMO system both with BPSK and QPSK modulations.

a) BPSK   b) QPSK
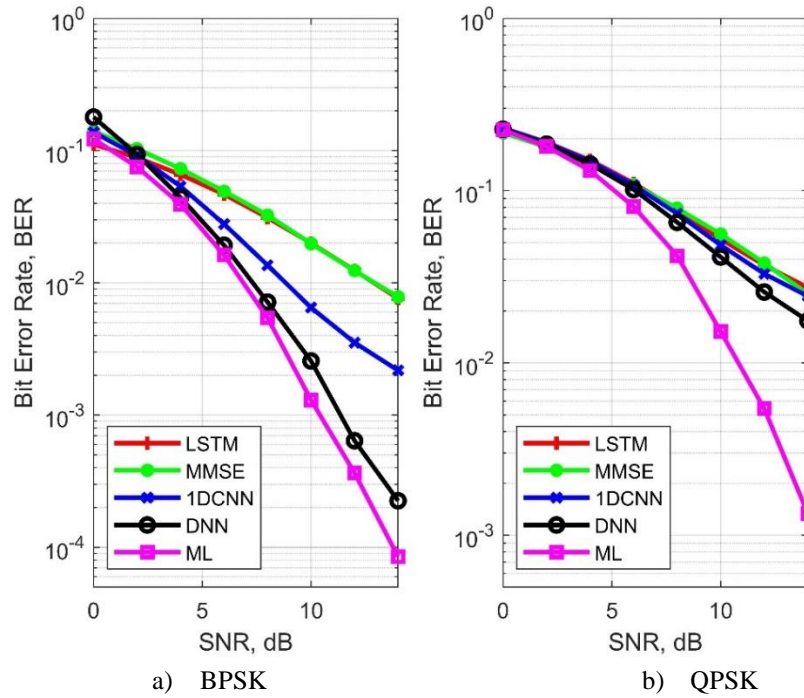
FIGURE 4. Bit error rate performance of detectors over 4x4 MIMO system.

As shown in Figure 4, performance of the DNN detector has a reasonable BER performance compared to the ML detector for BPSK modulation. For QPSK modulation DNN detector has still a higher detection performance than all other detectors except the ML detector. Nevertheless, DNN performance is not as high for QPSK as for BPSK modulation. The degradation of DNN performance for QPSK modulation depends on the increasing number of one-hot encoding labels which is related with the number of antennas and modulation order. We consider that by increasing the number of hidden layers and the number of layers in the DNN architecture, the degradation in the detection performance will vanish for the high order modulation case. Still, DNN has the best detection performance among the other DL based detectors for both BPSK and QPSK modulations and outperforms the MMSE detector.

In Figure 5, the bit error rate performances of the DNN, LSTM, 1DCNN, MMSE, and ML detectors for BPSK and QPSK modulations are given when the number of transmitter and receiver antennas are not equal to each other.

a)   8x4 MIMO with QPSK   b)   16x4 MIMO with BPSK
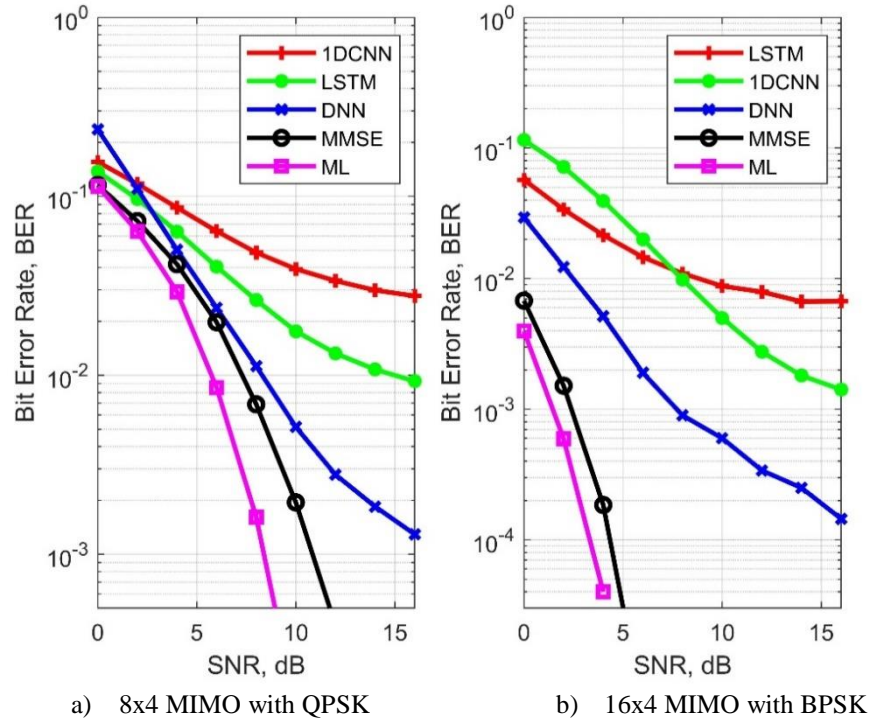
FIGURE 5. Bit error rate performance of detectors when the number of antennas is not equal.

In Figure 5, simulation results show that in the 8x4 MIMO system with QPSK modulation, the bit error rate performance of the DNN for low SNR values is close to that of the MMSE and ML detectors, while for high SNR values the performance of the DNN detector degrades. Moreover, performance of the DNN detector is not satisfactory for 16x4 MIMO system with BPSK modulation. On the other hand, DNN still has the best performance over 1DCNN and LSTM detectors for both systems.

Finally, in Figure 6 we consider a 2x2 MIMO system with 16-quadrature amplitude modulation (16-QAM) to compare the performance of the discussed detectors.
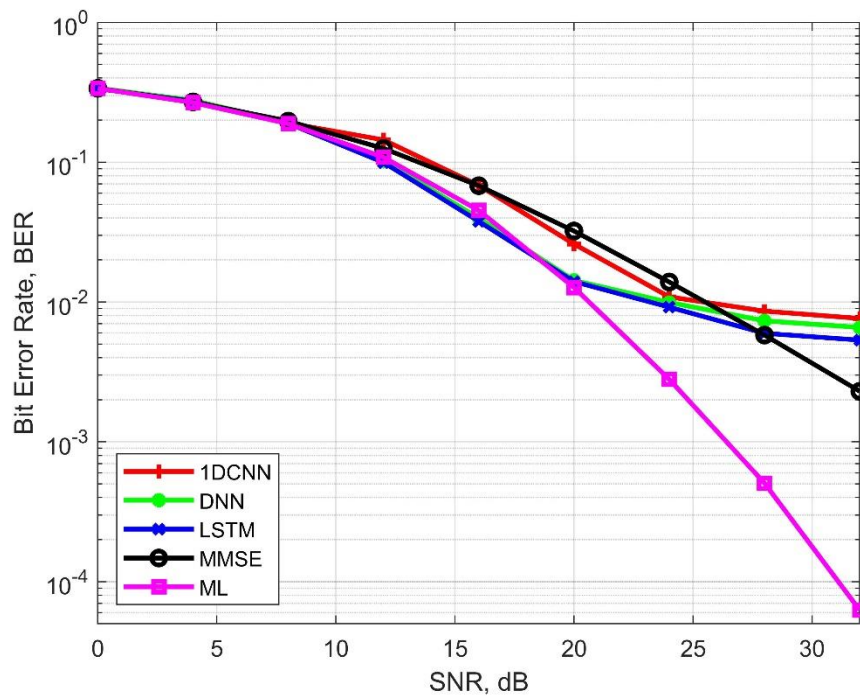
FIGURE 6. Bit error rate performance of detectors over 2x2 MIMO with 16-QAM.

The results in Figure 6 show significant differences from the results in the previous figures. As shown in Figure 6, although DNN, LSTM, and 1DCNN architectures give results close to optimal detector performance at low SNR, for high SNR values performance of the all DL based detectors decreases but still better than the MMSE detector for a limited range. The degradation of the detection performance of the DL based detectors can be explained by the increasing number of labels and complexity of the higher order modulation.

5. Conclusion

In this study, a conventional MIMO system is considered to show the detection performance of the different types of DL based detectors. In addition to a fully connected DNN architecture, performances of the LSTM and 1DCNN structures are discussed. Besides, well-known ML and MMSE detectors are utilized to compare the DL based detectors for different MIMO systems with various modulation types.

Simulation results show that DL based detectors have a detection performance close to the optimal ML detector and outperform the MMSE detector when the number of antennas and the modulation order is low. DNN architecture has the best detection performance compared to the performance of the LSTM and 1DCNN architectures. On the other hand, when the number of antennas and the modulation order are high, the detection performance of the DL based detectors may degrade.

The same parameters were employed in all simulations regardless of the difficulty of the problem to ensure the similar complexity of DL architectures. Therefore, the performance of the detectors can be improved by determining the appropriate network setting for each discussed scenario.

As a future study, the performance of the DNN detectors with different inputs for the input layer can be analyzed to improve the detection performance; however, the ultimate goal is to develop a deep learning detector based solely on the received signal.

Author Contribution Statements Authors are equally contributed to the paper. All authors read and approved the final copy of the manuscript.

Declaration of Competing Interests The authors declare that they have no known competing financial interests or personal relationships that could have appeared to influence the work reported in this paper.

References

[1] Yang, S., Hanzo, L., Fifty years of MIMO detection: The road to large-scale MIMOs, *IEEE Comm. Surv. Tutor.*, 17 (4) (2015), 1941-1988, https://doi.org/10.1109/COMST.2015.2475242.

[2] Albreem, M. A., Juntti, M., Shahabuddin, S., Massive MIMO detection techniques: A Survey, *IEEE Comm. Surv. Tutor.*, 21 (4) (2019), 3109-3132, https://doi.org/10.1109/COMST.2019.2935810.

[3] Wei, Y., Zhao, M-M., Hong, M., Zhao, M-J., Lei, M., Learned conjugate gradient descent network for Massive MIMO detection, *IEEE Trans. Signal Process.*, 68 (2020), 6336-6349, https://doi.org/10.1109/TSP.2020.3035832.

[4] Dai, L., Gao, X., Su, X., Han, S., I, C-L., Wang, Z., Low complexity soft-output signal detection based on Gauss-Seidel method for uplink multiuser large-scale MIMO systems, *IEEE Trans. Veh. Technol.*, 64 (10) (2015), 4839-4845, https://doi.org/10.1109/TVT.2014.2370106.

[5] Yu, A., Jing, S., Tan, X., Wu, Z. Yan, Z., Zhang, Z., You, X., Zhang, C., Efficient successive over relaxation detectors for massive MIMO, *IEEE Trans. Circuits Syst. I: Regul. Pap.*, 67 (6) (2020), 2128-2139, https://doi.org/10.1109/TCSI.2020.2966318 .

[6] LeCun, Y., Bengio, Y., Hinton, G., Deep learning, *Nature*, 521 (2015), 436-444, https://doi.org/10.1038/nature14539.

[7] Zhang, J., He, Y., Li, Y-W., Wen, C-K., Jin, S., Meta learning-based MIMO detectors: Design, simulation, and experimental test, *IEEE Trans. Wirel. Commun.*, 20 (2) (2021), 1122-1137, https://doi.org/10.1109/TWC.2020.3030882.

[8] Albreem, M. A., Alhabbash, A. H., Shahabuddin, S., Juntti, M., Deep learning for massive uplink detectors, *IEEE Comm. Surv. Tutor.*, 24 (1) (2022), 741-766, https://doi.org/10.1109/COMST.2021.3135542.

[9] Hershey, J. R., Roux, J. L., Weninger, F., Deep unfolding: Model-based inspiration of novel deep architectures, arXiv:1409.2574, (2014), https://doi.org/10.48550/arXiv.1409.2574.

[10] Balatsoukas-Stimming, A., Studer, C., Deep unfolding for communication systems: A survey and some new directions, *2019 IEEE International Workshop on Signal Processing Systems (SiPS)*, (2019), 266-271, https://doi.org/10.1109/SiPS47522.2019.9020494.

[11] Liao, J., Zhao, J., Gao, F., Li, G. Y., A model-driven deep learning method for massive MIMO detection, *IEEE Commun. Lett.*, 24 (8) (2020), 1724-1728, https://doi.org/10.1109/LCOMM.2020.2989672.

[12] He, H., Wen, C-K., Jin, S., L, G. Y., A model-driven deep learning network for MIMO detection, *2018 IEEE Global Conference on Signal and Information Processing (GlobalSIP)*, (2018), 584-588, https://doi.org/10.1109/GlobalSIP.2018.8646357.

[13] O'Shea, T. J., Erpek, T., Clancy, T. C., Deep learning-based MIMO communications, arXiv: 1707.07980, (2017), https://doi.org/10.48550/arXiv.1707.07980.

[14] Samuel N., Diskin, T., Wiesel, A., Learning to detect, *IEEE Trans. Signal Process.*, 67 (10), (2019), 2554-2564, https://doi.org/10.1109/TSP.2019.2899805.

[15] Baek, M-S., Kwak, S., Jung, J-Y., Kim, H. M., Choi, D-J., Implementation methodologies of deep learning-based signal detection for conventional MIMO transmitters, *IEEE Trans. Broadcast.*, 65 (3) (2019), 636-642, https://doi.org/10.1109/TBC.2019.2891051.

[16] Chen, Q., Zhang, S., Xu, S., Cao, S., Efficient MIMO detection with imperfect channel knowledge – A deep learning approach, *2019 IEEE Wireless Communications and Networking Conference (WCNC)*, (2019), 1-6,

https://doi.org/10.1109/WCNC.2019.8885582.

[17] Corlay, V., Boutros, J. J., Ciblat, P., Brunel, L., Multilevel MIMO detection with deep learning, *2018 52ⁿᵈ Asilomar Conference on Signals, Systems, and Computers*, (2018), 1805-1809, https://doi.org/10.1109/ACSSC.2018.8645519.

[18] Poudel, B., Oshima, J., Kobayashi, H., Iwashita, K., MIMO detection using a deep learning neural network in a mode division multiplexing optical transmission system, *Opt. Commun.*, 440 (2019), 41-48, https://doi.org/10.1016/j.optcom.2019.02.016.

[19] Lin, C., Chang, Q., Li, X., A deep learning approach for MIMO-NOMA downlink signal detection, *Sensors*, 19 (11) (2019), 2526, https://doi.org/10.3390/s19112526.

[20] Sun, J., Zhang, Y., Xue, J., Xu, Z., Learning to search for MIMO detection, *IEEE Trans. Wirel. Commun.*, 19 (11) (2020), 7571-7584, https://doi.org/10.1109/TWC.2020.3012785.

[21] Zappone, A., Renzo, M. D., Debbah, M., Wireless network design in the era of deep learning: Model-based, AI-based, or both?, *IEEE Trans. Commun.*, 67 (10) (2019), 7331-7376, https://doi.org/10.1109/TCOMM.2019.2924010.

A STUDY ON MODELING GROWTH MODEL OF ADANA PIGEONS

Levent ÖZBEK[1]

[1]Department of Statistics, Faculty of Science, Ankara University,
Ankara, TURKEY

ABSTRACT. The study aims to determine a mathematical model that can be used to describe the growth of the Adana pigeon. Since pigeons have only one breeding season, just one or two pairs of baby pigeons are raised per year. Hatchlings sometimes die before reaching adulthood. For this reason, measurements can be taken for 10, 15 and 60 days periods. Related with this issue, only 43-days measurements of 68 pigeons are used over a 6-year period. The study is modelled by taking the day-to-day average of the data (43 days) of 68 pigeons. The study was conducted on 68 Adana pigeons in the interval between the age of 1 and 43 days. The growth of pigeon cub was measured by daily live weight until 1 to 43 days. The estimation is carried out by writing the specific Matlab codes. Classical growth functions used in animals are in nonlinear form. Various numerical methods have been developed to estimate parameters in nonlinear functions. Special program routines have been developed to implement these methods. In these nonlinear models, there are more than one parameter to be estimated. Therefore, the number of mathematical operations in estimating the parameters is large. The most used models in the literature are Brody, Bertalanffy, Logistic, Generalized Logistic, Gompertz, Richards, Negative Exponential, Stevens, and Tanaka. However, as far as is known, there is no published article for Adana pigeons that uses all of these models and compares which one is better. These models are Brody, Bertalanffy, Logistic, Generalized Logistic, Gompertz, Richards, Negative Exponential, Stevens, and Tanaka. The best analysis was done by the Richards model in terms of both the Mean Squared Error (MSE), mean absolute percentage error (MAPE) and (Coefficient of Determination) R^2.

1. INTRODUCTION

Pigeons are among the species which played an important role in human history. First known as a religious symbol in the old times, they were then used as a means for transmitting messages during wars, and now it is a symbol of peace. Domestic pigeon species originated from *Columba livia* (rock pigeon), a kind of *Columba* species found in the *Columbinae* sub-family of the *Columbidae* family [1]. Genome

analysis was done by Shapiro et all [2]. The domestication time of pigeon cannot be exactly fixed [3-4].

Adana pigeons known as Adana dewlap over the world are known as Adana in Turkey. They are known as Adana wammen or earring dewlap in Germany. They are mainly raised in Çukurova Region. They are densely found in our settlements such as Adana, Ceyhan, Mersin, and Tarsus. Although in the sources there is some information related to the fact that they are originally descended from the Lebanon dewlaps (Lebanon races with dewlap), the truthiness of this information can be discussed because there is a clear difference between Adana pigeon and Lebanon dewlaps in terms of both physical appearance and flight characteristics. These pigeons which have gained a color, form, and flight characteristics special to themselves since the Ottoman period through the participation of different characteristics to the race by the raisers in Turkey, today, are also raised in Syria and known with Adana name even there. Adana pigeons are not raised for their colors. Color is not important at these pigeons. These pigeons are precisely performance birds. Adana pigeons have different characteristics from the other dewlaps in terms of flight characteristics. Their pike styles are especially different. Adana pigeons are not flown for long periods and in big groups. They are mostly flown in groups of three or four. Adana pigeons are kept in the closets consisting of small cells whose doors can be closed and where just two birds can fit into. The gate of the closet is kept closed at night. Each pair has its own cell in the closet [5].

The term "growth" is used to describe various biological phenomena. Growth of populations involves the reproduction of animals; growth of bodies involves an increase in the number of cells or growth in the size of cells; the growth of cells involves molecular replication. In a more broad sense, growth indicates a development in mass due to an increase in size and number of living things. The growth of organic structures is distinct from the growth of crystal structures in inorganic substances. Growth in organic structures, or more precisely living things, is the result of an increase in the height and weight of a single organism, a tissue or an organ due to a combination of biological and biochemical events, or it is the result of an increase in the number of members in a population formed by organisms. It is observed that the growth curves are commonly used for modelling the progress of the virus since it is the field of study for microbiologists. Growth curves are used for modelling the increase in the number of plants, bacteria or viruses in an environment. Expressing the growth of an organism or the increase in the number of viruses temporally is called "growth". The identification of the complex growth process is aimed at using the growth curves [6-8].

The Gompertz Model (GM) is well known and widely used in many sub-fields of biology [9-10]. Numerous parametrizations and re-parametrizations of the GM may be found in the literature [11]. The use of mathematical population models as the

basis for analysis on time series population abundances has been a productive and useful area of research in the past decade [12-28]. The models discussed in these studies are static nonlinear growth models. The models employed in those papers are non-linear mathematical growth models and there are more than one parameter to be estimated in those models. The models are non-linear mathematical models and defined using differential equations. Specific algorithms such as mathematical optimization technique need to be employed for parameter estimation. The data used in the models employed need to be updated daily in order to analyze it. The methods used are offline and all data up to a spesific date is needed for parameter estimation in those models where the estimation needs to be updated on a daily basis with the inclusion of the new set of data. There are other growth models is addition to Logistic, Bertalanffy and Gompertz non-linear mathematical models and they are given in the Table 1.

TABLE 1. Non-linear models and their mathematical notations.

Model name	Statistical model
Brody	$y(t;\alpha,\beta,k)=\alpha(1-\beta\exp(-kt))+\varepsilon$
Bertalanffy	$y(t;\alpha,\beta,k,m)=(\alpha^{1-m}-\beta\exp(-kt))^{1/(1-m)}+\varepsilon$
Logistic	$y(t;\alpha,\beta,k)=\alpha/(1+\beta\exp(-kt))+\varepsilon$
Generalized Logistic	$y(t;\beta,k,\gamma)=\alpha/((1+\beta\exp(-kmt)^{1/m})+\varepsilon$
Richards	$y(t;\alpha,k,m)=\alpha(1-\exp(-kt))^{1/m}+\varepsilon$
Negative Exponential	$y(t;\alpha,k)=\alpha(1-\exp(-kt))+\varepsilon$
Stevens	$y(t;\alpha,\beta,p)=\alpha-\beta(k^t)+\varepsilon$
Tanaka	$y(t;\alpha,\beta,k,m)=(1/\sqrt{\beta})\ln|2\beta.(t-m)+2\sqrt{k^2(t-m)^2+\alpha\beta}|+\varepsilon$
Gompertz	$Y(t)=\alpha\exp(-\beta\exp(-kt))+\varepsilon$

2. MATERIAL AND METHOD

The study was conducted on 68 Adana pigeons in the interval between the age of 1 and 43 days. The parameter estimation is done related to the daily weight averages of 68 pigeons. In this study, MSE, MAPE and R^2 statistics are used for making a comparison between the models to determine best fitted model. We use MSE, MAPE, and R^2 statistics for all models that are given in Table 2. As seen in Table 2, R^2 values are resulted as being close to each other. Nevertheless, it may be stated that the Richards model is the most consistent in terms of both MAPE, and MSE.

The best analysis has been made by the Richards model in terms of both MAPE and MSE. Actual values and estimated values using the Richard model is given in Fig. 1. As a result of estimation acquired by data the best analysis for modelling the growth is made by the Richards model in terms of both MAPE and MSE. It has been determined that the use of this model is appropriate.

TABLE 2. MSE, MAPE and R^2 values regarding the models.

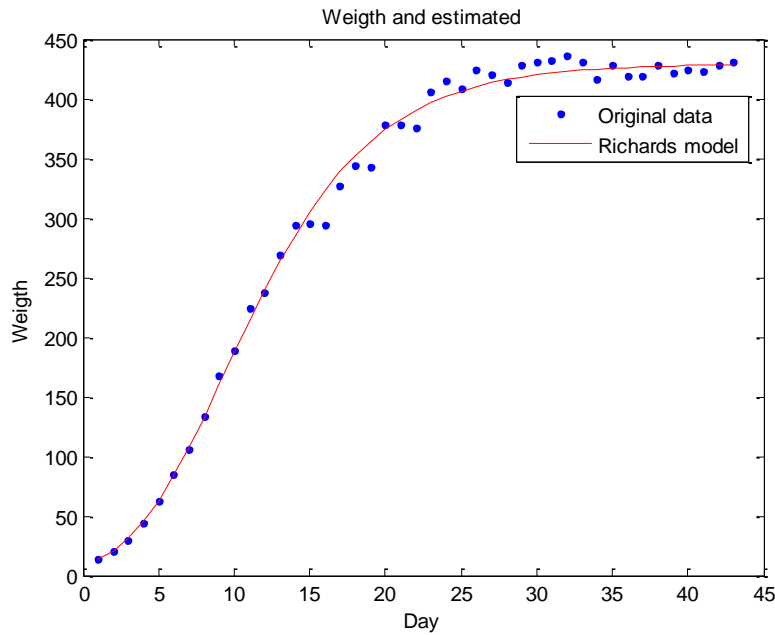| Model	MSE	R^2	MAPE
Brody	88.6383	0.9955	1.2851
Bertalanffy	88.6378	0.9955	1.2851
Logistic	180.2924	0.9908	1.5434
Generalized Logistic	1.0141	0.9999	6.5335
Gompertz	92.5197	0.9953	0.9886
Richards	**80.8354**	**0.9959**	**0.9807**
Negative Exponential	1200	0.9955	6.1198
Stevens	88.6378	0.9999	1.2851
Tanaka	4133	0.5663	19.9527

FIGURE 1. Richards model: Original data and estimated data.

3. DISCRETE-TIME GOMPERTZ MODEL (DTGM)

In the article in reference [29], the authors use a discrete-time stochastic Gompertz model for the weight of the pigeon which are encountered until t day(s). Let n_t denote the weight of the pigeon at time t. The process model is as:

$$n_t = n_{t-1} \exp(a + b \ln n_{t-1} + e_t). \tag{1}$$

Where, a and b are constants, and e_t is a random variable distributed as $e_t \sim N(0, \sigma_1^2)$. The random variables $e_1, e_2, ..., e_n$ are assumed to be uncorrelated. On the logarithmic scale, the DTGM is a linear autoregressive time-series model of order 1 [AR(1) process] defined as equation 2.

$$y_t = y_{t-1} + a + by_{t-1} + e_t = a + cy_{t-1} + e_t \tag{2}$$

where, $y_t = \ln n_t$ and $c = b + 1$. For statistical properties of DTGM, see [18]. The model has a long history in density-dependence modeling see [30-32]. A frequently seen alternative is a stochastic version of the Moran-Ricker model [32], which uses n_{t-1} instead of $\ln n_{t-1}$ in the exponential function; in comparative data analysis studies, the Gompertz model has performed as well as the Moran-Ricker [31]. The probability distribution of n_{t-1} is a normal distribution with mean and variance that change as functions of time. If $-1 < c < 1$, the probability distribution of n_t eventually approaches a time-independent stationary distribution that is a normal distribution with a mean of $a/(1-c)$ and a variance of $\sigma_1^2/(1-c^2)$. The stationary distribution is the stochastic version of an equilibrium in the deterministic model, and is an important statistical manifestation of density dependence in the population growth model Dennis [18]. In equation 4, a is the intrinsic growth rate, b is the density-dependent influence [31].

In the article in reference [29], Kalman Filter[1] has been used to estimate the time-varying parameter of the DTGM. KF is a recursive estimator to estimate the time-

---

[1] Kalman filter is in fact an estimator rather than a conventional filter, however it is employed to estimate parameters from a noisy data sequence, hence the name filter.

varying parameters. If $a = 0$ in Eq.(2), n_t takes the case counts observed until t and $y_t = \ln n_t$. Then the equation

$$y_t = c y_{t-1} + e_t \tag{3}$$

is acquired. In the case that the parameter c in Eq.(5) is time-varying and presumed as random walk process, that is $c_t = c_{t-1} + w_t$. Then state-space model,

$$y_t = c_t y_{t-1} + e_t \tag{4}$$

$$c_t = c_{t-1} + w_t \tag{5}$$

is obtained and w_t is distributed as $w_t \sim N(0, \sigma_2^2)$. The random variables $w_1, w_2, ..., w_n$ are assumed to be uncorrelated. Here, the state variable c_t is unobservable, time-varying, and can be estimated through adaptive Kalman Filter (AKF). If this time-varying parameter is estimated using on-line AKF, estimation for the growth in times $t+1$, $t+2$, ... can be made via this online-estimated parameter. According to the estimation results obtained by using the daily weight measurements in the DTGM, MSE, MAPE, and R^2 were calculated (see Table 2).

TABLE 3. Values of MSE, MAPE, R^2.

	MSE	R^2	MAPE
Weight	270	0.9861	2.3045

4. RESULTS AND DISCUSSION

Classical growth functions used in animals are in nonlinear form. Various numerical methods have been developed to estimate parameters in nonlinear functions. Special program routines have been developed to implement these methods. In these nonlinear models, there are more than one parameter to be estimated. Therefore, the number of mathematical operations in estimating the parameters is large.

The most used models in the literature are Brody, Bertalanffy, Logistic, Generalized Logistic, Gompertz, Richards, Negative Exponential, Stevens, and Tanaka.

However, as far as is known, there is no published article for Adana pigeons that uses all of these models and compares which one is better.

The study is modelled by taking the day-to-day average of the data (43 days) of 68 Adana pigeons. The study was conducted on 68 Adana pigeons in the interval between the age of 1 and 43 days.

These models are Brody, Bertalanffy, Logistic, Generalized Logistic, Gompertz, Richards, Negative Exponential, Stevens, and Tanaka.

The best analysis was done by the Richards model in terms of both the Mean Squared Error (MSE), mean absolute percentage error (MAPE) and (Coefficient of Determination) R^2.

Considering the measurements in Table 2 and Table 3, it is seen that the Richards model discussed in this study represents the data better when compared to the results obtained in the article in reference [29].

This article is an initial study on research Adana pigeons. Our studies continue on models that use time series methods to model the growth dynamics of Adana pigeons, which are not included in the literature.

Declaration of Competing Interests The author declare that he has no known competing financial interests or personal relationships that could have appeared to influence the work reported in this paper.

REFERENCES

[1] Secord, J. A., Nature's fancy: Charles Darwin and the breeding of pigeons, *Isis*, 72 (2) (1981), 162-186.

[2] Shapiro, M., Genomic diversity and evolution of the head crest in the rock pigeon, *Science*, 339 (6123) (2013), 1063-1067, https://doi.org/10.1126/science.1230422.

[3] Yılmaz, O., Ertuğrul, M., Importance of pigeon husbandry in history, *J.Agric. Fac. HR.U.*, 16 (2) (2012), 1-7.

[4] Yılmaz, O., Savaş, S., Ertuğrul, M., Pigeon and pigeon rearing in the Turkish culture, *Nevşehir Üniversitesi Fen Bilimleri Enstitü Dergisi*, 2 (2012), 79-86.

[5] https://guvercinadana.tr.gg/, Accessed: 08.08.2020

[6] Gompertz, B., On the nature of the function expressive of the law of human mortality, and on a new mode of determining the value of life contingencies, *Philos. Trans. R. Soc.*, 115 (1825), 513-583.

[7] Bertalanffy, L., Problems of organic growth, *Nature*, 163 (1949), 156-158, https://doi.org/10.1038/163156a0.

[8] Richards, F. A., Flexible growth function for empirical use, *J. Exp. Bot.*, 10 (1959), 290-301, https://doi.org/10.1093/jxb/10.2.290.

[9] Zwietering, M., Jongenburger, I., Rombouts, F., Van't, R. K., Modeling of the bacterial growth curve, *Appl. Environ. Microbiol.*, 56 (6) (1990), 1875-1881, https://doi.org/10.1128/aem.56.6.1875-1881.1990.

[10] Gerlee, P., The model muddle: in search of tumor growth laws, *Cancer Res.,* 73 (8) (2013), 2407-2411, https://doi.org/10.1158/0008-5472.CAN-12-4355.

[11] Kathleen, M. C., Tjørve, E., The use of Gompertz models in growth analyses, and new Gompertz-model approach: An addition to the unified-Richards family, *PLOS ONE*, 12 (6) (2017), 1-17, https://doi.org/10.1371/journal.pone.0178691.

[12] Topal, M., Ozdemir, M., Aksakal, V., Yildiz, N., Dogru, U., Determination of the best non-linear function in order to estimate growth in Morkaraman and Awassi lambs, *Small Rumin. Res.*, 55 (2004), 229-232, https://doi.org/10.1016/j.smallrumres.2004.01.007.

[13] Şengul, T., Kiraz, S., Non-linear models for growth curves in large white turkeys, *Turk. J. Vet. Anim. Sci.*, 29 (2005), 331-337.

[14] Sezer, M., Tarhan, S., Model parameters of growth curves of three meat-type lines of Japanese quail, *Czech J. Anim. Sci.*, 50 (2005), 22-30, https://doi.org/10.17221/3991-CJAS.

[15] Kizilkaya, K., Balcioglu, M., Yolcu H., Karabag, K., Genc I., Growth curve analysis using nonlinear mixed model in divergently selected Japanese quails, *EPS*, 70 (2006), 181-186.

[16] Topal, M., Bolukbasi, Ş., Comparison of nonlinear growth curve models in broiler chickens, *J. App. Anim. Res.*, 34 (2008), 149-152, https://doi.org/10.1080/09712119.2008.9706960.

[17] Gbangboche, A. B., Glele, K. R., Salifou, S., Albuquerque, L. G., Comparison of non-linear growth models to describe the growth curve in West African Dwarf sheep, *Animal*, 2 (2008) 1003-1012, https://doi.org/10.1017/S1751731108002206.

[18] Narinc, D., Karaman, E., Firat, M. Z., Aksoy, T., Comparison of nonlinear growth models to describe the growth in Japanese quail, *J. Anim. Vet. Adv.*, 9 (2010), 1961-1966.

[19] Özçelik, R., Yavuz, H., Karatepe, Y., Gürlevik, N., Kırış, R., Development of ecoregion-based height–diameter models for 3 economically important tree species of southern Turkey, *Turk. J. Vet. Anim. Sci.*, 38 (2014), 399-412.

[20] Ghaderi, Z. M., Rafeie, F., Bahreini, B. M. R., Simple hierarchical and general nonlinear growth modeling in sheep", *Turk. J. Vet. Anim. Sci.*, 42 (2018), 326-334.

[21] Faraji, A. H., Rokouei, M., Ghazaghi, M., Comparative study of growth patterns in seven strains of Japanese quail using nonlinear regression modeling, *Turk. J. Vet. Anim. Sci.*, 42 (2018), 441-451.

[22] Sariyel, V., Aygun, A., Keskin, I., Comparison of growth curve models in partridge, *Poult. Sci.*, 96 (2017), 1635-1640, https://doi.org/10.3382/ps/pew472.

[23] Ramos, S. B., Caetano, S., Savegnago, R. P., Nunes, B.N., Ramos, A. A., Munari. D. P., Growth curves for ostriches (*struthio camelus*) in a Brazilian population, *Poult. Sci.*, 92 (2013) 277-282, https://doi.org/10.3382/ps.2012-02380.

[24] Gon, A., Gotuzzo, C., Piles, M., Pillon, R., Genetics and genomics, Bayesian hierarchical model for comparison of different nonlinear function and genetic parameter

estimates of meat quails, *Poult. Sci.*, 98 (2019), 1601-1609, https://doi.org/10.3382/ps/pey548.

[25] Aggrey, S. E., Comparison of three nonlinear and spline regression models for describing chicken growth curves, *Poult. Sci.*, 81 (2002), 1782-1788, https://doi.org/10.1093/ps/81.12.1782.

[26] Kuhleitner, M., Brunner, N., Nowak, W.G., Best-fitting growth curves of the von Bertalanffy type, *Poult. Sci.*, 98 (2019), 3587-3592, https://doi.org/10.3382/ps/pez122.

[27] Gao, C. Q., Yang, J. X., Chen, M. X., Yan, H. C., Wang, X. Q., Growth curves and age-related changes in carcass characteristics, organs, serum parameters, and intestinal transporter gene expression in domestic pigeon (Columba livia), *Poult. Sci.*, 95 (2016) 867-877, https://doi.org/10.3382/ps/pev443.

[28] Vincek, D., Kralik, G., Kušec, G., Sabo, K., Scitovski, R., Application of growth functions in the prediction of live weight of domestic animals, *CEJOR*, 20 (2012), 719-733, https://doi.org/10.1007/s10100-011-0199-2.

[29] Özbek, L., A study on a new estimating growth model of Adana pigeons using discrete-time stochastic Gompertz model and adaptive Kalman filter, *Gazi Univ. J. Sci.*, in press, (2022).

[30] Reddingius, J., Gambling for existence: A discussion of some theoretical problems in animal population ecology, E. J. Brill, Leiden, 1971.

[31] Pollard, E., Lakhani, K. H., Rothery, P., The detection of density-dependence from a series of annual censuses, *Ecology*, 68 (1987), 2046-2055, https://doi.org/10.2307/1939895.

[32] Dennis, B., Taper, M. L., Density dependence in time series observations of natural populations: estimation and testing, *Ecol. Monogr.*, 64 (1994), 205-224.

DETERMINATION OF THE SURFACE TOPOGRAPHY IN RILL EROSION BY IMAGING TECHNIQUES

Kürşad ERDOĞAN[1] and Fikret ARI[1]

[1]Department of Electrical and Electronics Engineering,
Ankara University, Ankara, TURKEY

ABSTRACT. Soil erosion, mainly occurring in agricultural areas, is an economic and ecological problem that can happen anywhere. Swelling and transport of soil particles reduce the productivity of agricultural lands. Soil surface analysis and soil-water interaction are essential topics in agricultural research and engineering as they affect the risk of soil erosion. Erosion affects the upper soil layers rich in organic matter. After the transport of this topsoil, the subsoil with a more compact structure emerges. In this case, the cultivation of the soil becomes complex, and agricultural productivity is adversely affected. Different techniques have been used to analyze the effects of erosion. In this study, we focused on rill erosion, one of the types. An electronic imaging system has been designed using the Microsoft Kinect Sensor and Raspberry Pi, which can be found quickly and at a low cost during operation. The software has been developed to extract the surface topography by analyzing the depth images of rill erosion obtained with this system. Measurements were taken using eight types of flow rates on four soil types. As a result of the experimental findings, it has been seen that volume changes of 1.3812 mm^3 can be detected as a unit with the Kinect Sensor placed at a distance of 70 cm.

1. INTRODUCTION

Erosion is the carrying and sweeping of the soil by flood waters and winds from other external forces, especially rivers. Soil erosion, especially in agricultural areas, is an economic and ecological problem that can occur anywhere. Swelling and transport of soil particles reduce farmland productivity [1]. Soil surface analysis and soil-water interaction are essential topics in agricultural research and engineering as they affect the risk of soil erosion [2]. Erosion affects the upper soil layers rich in

organic matter. After the transport of this topsoil, the subsoil with a more compact structure emerges. In this case, soil cultivation becomes difficult, and agricultural productivity is adversely affected.

One of the forms of soil erosion, mainly caused by precipitation or water accumulation, is rill erosion. It is a type of erosion that occurs in the form of small channels formed by the collection of stream water, initiating a flow from weak and loose areas in the soil and dragging the soil during this flow [3]. When examining the damages caused by soil erosion, it is imperative to analyze the topography, which is the shape of the details of the land surface.

Many techniques have been developed for topography analysis. Terrestrial Laser Scanners [4], LiDAR (Light Detection and Ranging) [2], Unmanned Aerial Vehicles [3], and Digital cameras [5] were used to extract the topography.

It is considered that Microsoft Kinect-style depth sensing units and portable mini computer systems such as Raspberry Pi can be used in soil erosion analysis due to their low cost and ease of use. It is thought that the obtained topography results will positively contribute to protecting agricultural lands and increasing their productivity.

Raspberry Pi has been used in this study because of its flexible programming, small size, cheapness, and ease of supply. With the Python software developed on Raspberry Pi, depth images, including distance information, were obtained via Kinect Sensor. The topographies of rill-eroded areas on these images were extracted using image processing algorithms with MATLAB software. The extracted topography was analyzed, and evaluations were made on the soil losses after erosion.

A cheaper and more practical solution has been developed using mobile technologies to obtain a depth image using the Raspberry Pi and Kinect Sensor. Depth images can be obtained remotely by connecting to Raspberry Pi with mobile phones. Figure 1 shows the Python application running on a mobile phone with an Android operating system. Contribution of this paper, a simple and cost-effective system is proposed to analyze the effect of rill erosion.

2. Material and Methods

2.1. **Structure of the Developed System.** The system in Figure 2 is designed to extract the topography of rill erosion. Python libraries were installed on Raspberry Pi, and Python software was developed to take depth images via Kinect Sensor. Using the depth images obtained with developed software, the surface topography was obtained using image processing techniques with MATLAB software.
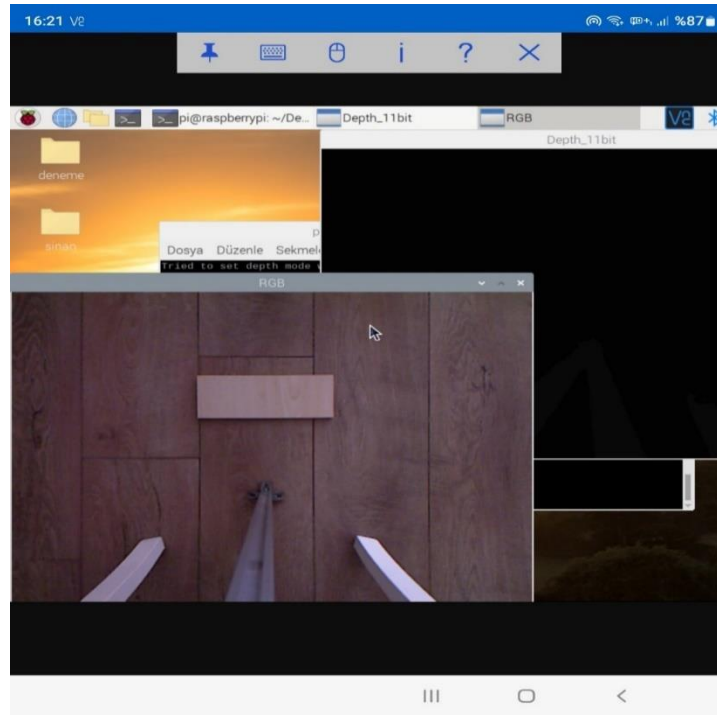
FIGURE 1. Depth and RGB image acquisition via Mobile Phone.
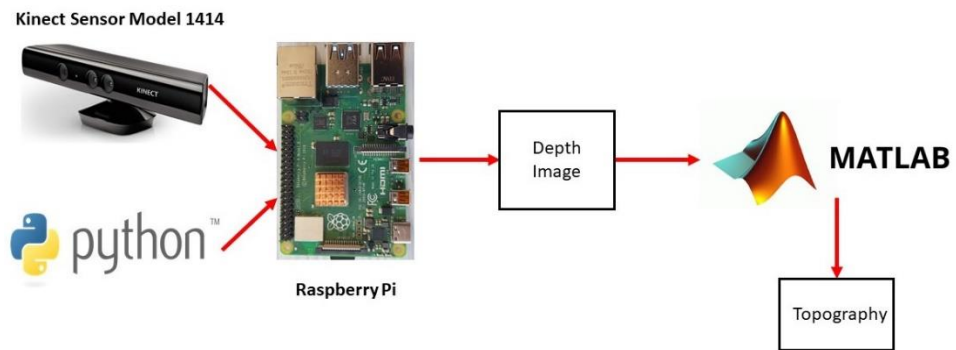
FIGURE 2. Designed system.

2.2. **Experimental Measuring Setup.** The mechanism was prepared in the Mechanical Production Laboratory and Electronics Development and Research Laboratory in the Department of Electrical and Electronics Engineering at Ankara University. This mechanism is the "Rill Erosion Measuring Device," which can also be expressed as a V-shaped small groove measurement setup created to measure the properties of soils against rill erosion at different flow values in the laboratory environment [6]. The Kinect Sensor was placed at a height 70 cm from the Rill Erosion Measuring Mechanism, and its connection with the Raspberry Pi was ensured. Depth images were taken by connecting a computer or mobile phone with a Raspberry Pi via Wi-Fi access. The experimental setup created is shown in Figure 3.

Raspberry Pi is Linux-based hardware developed for simple computer science learning. It has started to be used widely because it can perform most functions that a computer can do, can be programmed for different purposes, and is small in size and affordable. Raspberry Pi 4 Model B was used in the experimental study.

Kinect Sensor is a product initially developed by Microsoft for motion detection for the Xbox game console. With the microphone, RGB camera, depth sensor, and cheap cost, this product has started to be used for many applications besides being an additional device for a game console. Studies have been carried out on its usability for many applications, thanks to its hardware that allows real-life applications to be developed [7]. Kinect Sensor's RGB camera produces 8-bit video with a resolution of 640x480 pixels. The IR camera can create an 11-bit depth image with a resolution of 640x480 pixels [8].
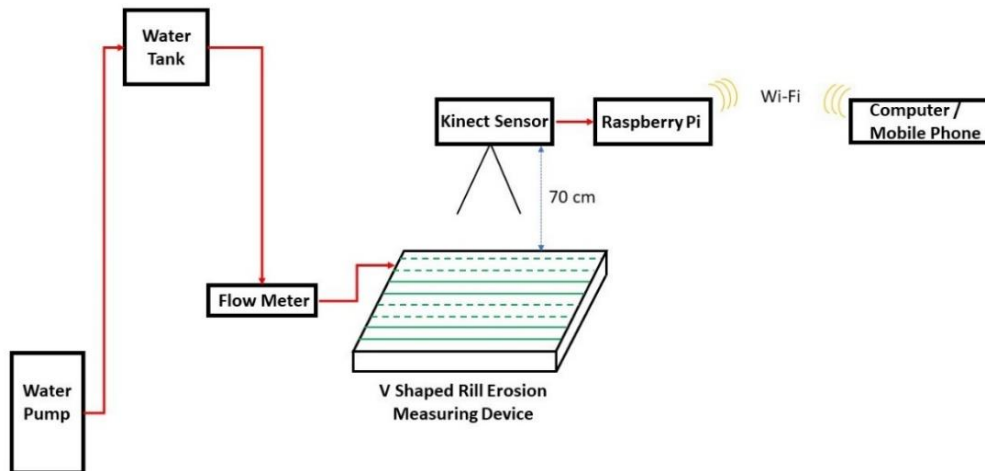
FIGURE 3. Experimental setup.

The raw values in the depth images obtained with the Kinect Sensor must be converted to values containing distance information in mm. For each pixel value, the distance value in mm is calculated by using the formulation in Equation 1 [9] with MATLAB program.

$$Distance = 1000 * \left[k1 * \tan\left(\frac{RawDepth}{k2} + k3\right) \right] \tag{1}$$

The coefficients used in Equation 1 are k1 = 0.1236, k2 = 2,842.5, k3 = 1.1863.

Kinect Sensor makes IR radiation with the IR projector. The IR camera detects the reflection of this IR radiation from the environment. The Kinect Sensor creates depth images through the relationship between this radiation and reflection. Various noises may also occur in the depth images created by the Kinect Sensor. In the experimental studies, "Unmeasurable Depth" noises, where the depth value cannot be measured, may occur in the depth calculation of the objects located very close to or far from the Kinect Sensor. This may appear due to discontinuities on the surface, reflections, shadows, or other reasons [10].

To eliminate the immeasurable depth noise on the depth images containing the distance information obtained, it is necessary to search for this error in each pixel of the 640x480 pixel image and take action to correct the defective pixel. For this, a 5x5 filter was used on the image.
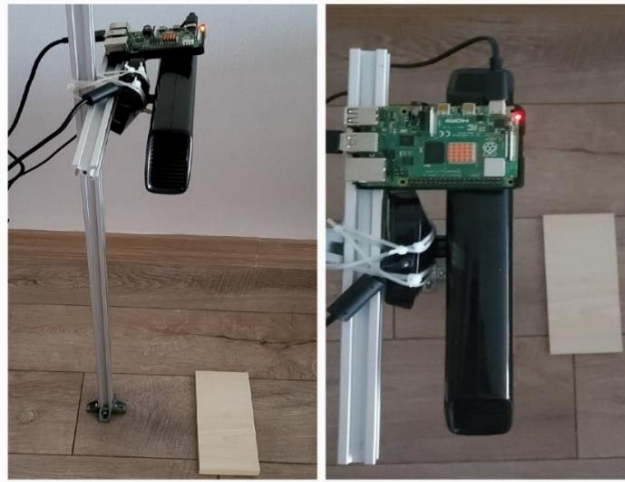
FIGURE 4. Test setup designed for the creation of the reference table.

After all these processes, it is necessary to calculate how much surface area each pixel in the surface topography corresponds to. The test setup in Figure 4 was prepared to create a reference table based on the distance of the Kinect Sensor to the relevant surface. Depth images were taken over the reference object by placing the Kinect Sensor at 1 cm distances between 70 cm and 80 cm. The area of the real object is divided by the area of the depth image in pixels. The reference table in Table 1 was created with the calculated values.

The actual volume of the object used in Figure 4 was calculated with the designed setup with a difference of 5.8 mm^3 (Table 2).

TABLE 1. Reference table.

Distance of Kinect Sensor to Object (cm)	Total Number of Pixels	Area Corresponding to 1 Pixel (mm^2)
70	13,698	1.3812
71	13,433	1.4085
72	12,894	1.4674
73	12,799	1.4782
74	12,283	1.5403
75	12,009	1.5755
76	11,697	1.6175
77	11,637	1.6259
78	11,027	1.7158
79	11,026	1.7159
80	10,681	1.7714

3. Results and Discussion

Rill erosion was created by placing four types of soil, shown in Figure 5, into the V-shaped rill erosion measurement setup, and flowing water at a flow rate of 0.10, 0.20, 0.30, 0.40, 0.50, 0.60, 0.70, and 0.80 for 3 minutes for each.

TABLE 2. Test results.

Reference			MATLAB Measurement
Vertical (mm)	86	Total Pixels	13,698
Horizantal (mm)	220	Unit Area (mm^2)	1.3812
Height (mm)	18	Height (mm)	18
Volume (mm^3)	340,560	Volume (mm^3)	340,554.20

FIGURE 5. Soil types used in experimental study.

Information on the regions from which soil samples were taken and used in the experimental study is given in Table 3.

Rill erosion was created at the flow as mentioned above rates for each soil type, respectively. The RGB image was taken with a digital camera (a mobile phone with an Android operating system). Depth images were taken with the Kinect Sensor. An example of the captured images is given in Figure 6.

TABLE 3. Information on the region where the soil sample was taken.

| Type of Soil | City / Town | Coordinates | | Land Use |
		Y	X	
S1 (Clay Soil)	Ankara/Ayaş	36449767E	4444604N	Plowed land (garden)
S2 (Silty Clay Soil)	Ankara/Polatlı	36427979E	4351404N	Plowed wheat stubble
S3 (Silty Clay Soil)	Ankara/Polatlı	36429841E	4350492N	Plowed land (garden)
S4 (Clay Soil)	Ankara/Polatlı	36423323E	4353041N	Sugar beet field
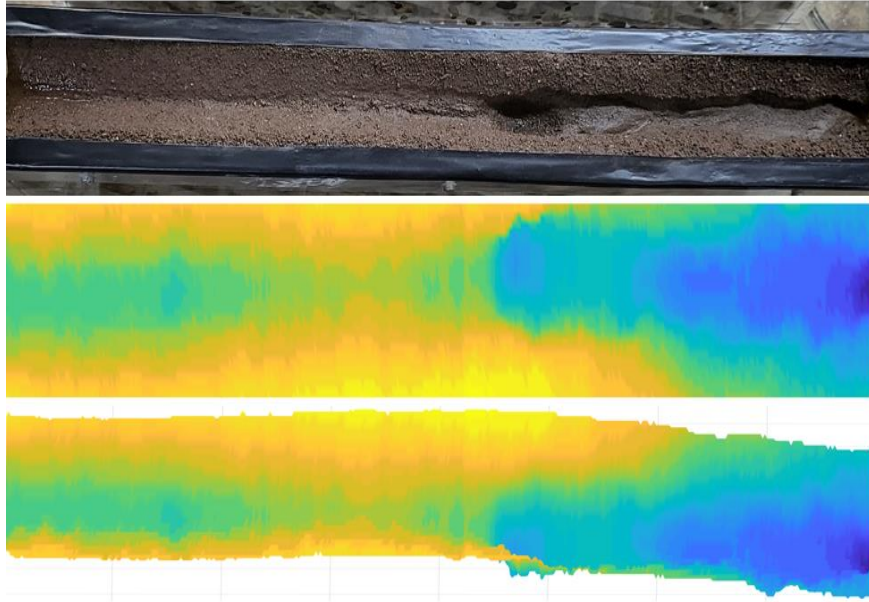
FIGURE 6. Soil 2, image after 0.80 flow.
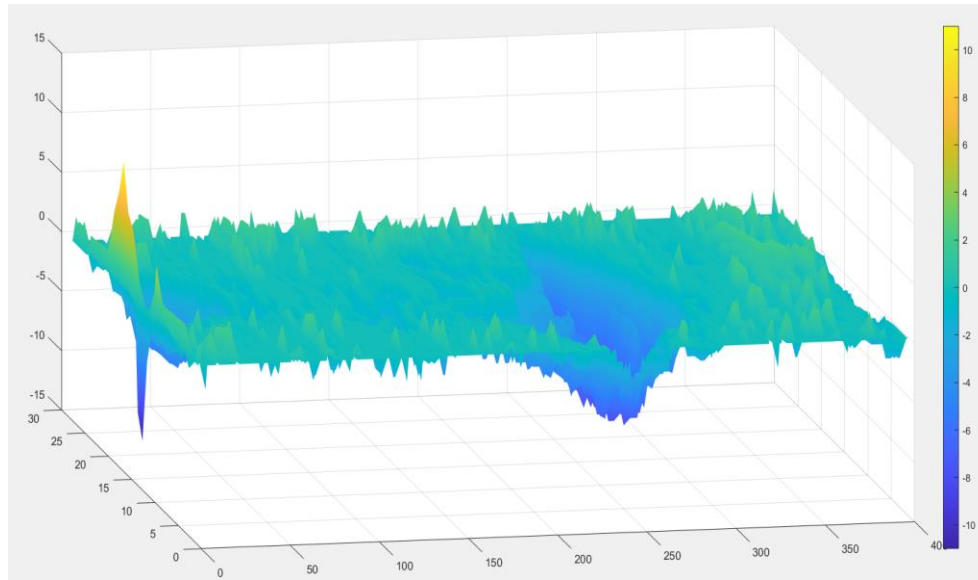
FIGURE 7. Soil 4, Comparison of soil movements between 0.10 – 0.80 flow rate.

To calculate the soil losses after the water flows on the soil samples, the surface topographies obtained as a result of both flows were subtracted from each other, and different images were obtained. The difference images of the depth images formed after 0.10 flow and 0.80 flow water flow were obtained to control the calculations. An example of the calculated difference images is given in Figure 7.

As seen in Figure 3, the Kinect Sensor is placed at the height of 70 cm. When calculating the lost soil volume, the difference between pixels with negative values and pixels with positive values is taken. The resulting difference in pixel value gives the height values in mm to be included in the volume calculation. The volume value of the lost soil was calculated by multiplying each pixel value (height) with the area value of 1.3812 mm^2 corresponding to 70 cm in the reference table in Table 1.

During erosion, soil loss occurs due to water flow. Depending on the characteristics of the soil type used, displacement of the soil without loss due to water entrainment and swelling of the soil with water may also occur. Negative values in Figure 7 indicate soil loss and positive values indicate soil areas that have been transported or swelled by water.

The volume calculations for the soil losses calculated depending on the soil types are shown in Tables 4 and 5 below.

When examining the difference between 0.20 and 0.30 flow rates for Soil 1, the

amount of soil loss due to erosion was less than soil movement or swelling. The amount of lost soil is calculated between flow rates; when the difference between the initial flow (0.10 flow) and the final flow (0.80 flow) is compared with the soil loss, it is seen that the difference is only 0.28 mm^3.

The amount of lost soil calculated between flow rates for Soil 2. When the difference between the initial flow (0.10 flow) and the final flow (0.80 flow) is compared with the soil loss, it is seen that the difference is only 0.21 mm^3.

The amount of lost soil is calculated between flow rates for Soil 3. When the difference between the initial flow (0.10 flow) and the final flow (0.80 flow) is compared with the soil loss, it is seen that the difference is only -0.01 mm^3.

When examining the difference between 0.10 and 0.20 flow rates and 0.60 and 0.70 flow flows for Soil 4, the amount of soil loss due to erosion was less than soil movement or swelling. The amount of lost soil is calculated between flow rates; when the difference between the initial flow (0.10 flow rate) and the final flow (0.80 flow) is compared with the soil loss, it is seen that the difference is only -0.09 mm^3.

TABLE 4. Rill erosion soil loss analysis (Soil 1 and 2).

Flows	Soil 1			Soil 2		
	Loss Soil (mm^3)	Carrying or Sweeping Soil (mm^3)	Total Loss Soil (mm^3)	Loss Soil (mm^3)	Carrying or Sweeping Soil (mm^3)	Total Lost Soil (mm^3)
0.10-0.20	3,436.40	1,041.40	2,395.00	4,606.30	2,558.00	2,048.30
0.20-0.30	2,250.00	5,588.30	-3,338.30	4,215.40	701.65	3,513.75
0.30-0.40	5,908.80	483.42	5,425.38	2,292.80	366.02	1,926.78
0.40-0.50	17,291.00	3,375.70	13,915.30	1,780.40	993.09	787.31
0.50-0.60	5,522.00	1,421.30	4,100.70	3,935.00	946.12	2,988.88
0.60-0.70	12,224.00	1,831.50	10,392.50	5,777.60	871.54	4,906.06
0.70-0.80	18,362.00	1,436.40	16,925.60	8,465.40	2,808.00	5,657.40
		Total	49,816.18		Total	21,828.48
0.10-0.80	51,146.00	1,330.10	49,815.90	22,715.00	886.73	21,828.27
		Difference	0.28		Difference	0.21

TABLE 5. Rill erosion soil loss analysis (Soil 3 and 4).

Flows	Soil 3			Soil 4		
	Loss Soil (mm³)	Carrying or Sweeping Soil (mm³)	Total Loss Soil (mm³)	Loss Soil (mm³)	Carrying or Sweeping Soil (mm³)	Total Lost Soil (mm³)
0.10-0.20	5,678.10	1,296.90	4,381.20	932.31	2,769.30	-1,836.99
0.20-0.30	4,320.40	2,466.80	1,853.60	3,366.00	1,379.80	1,986.20
0.30-0.40	6,348.00	2,248.60	4,099.40	4,838.30	1,256.90	3,581.40
0.40-0.50	7,794.10	2,839.70	4,954.40	4,917.10	1,975.10	2,942.00
0.50-0.60	7,165.70	2,006.90	5,158.80	2,977.90	1,370.20	1,607.70
0.60-0.70	5,180.90	1,426.80	3,754.10	2,298.30	2,342.50	-44.2
0.70-0.80	5,857.70	3,575.90	2,281.80	6,798.30	1,134.00	5,664.30
		Total	26,483.30		Total	13,900.41
0.10-0.80	27,388.00	904.69	26,483.31	15,301.00	1,400.50	13,900.50
		Difference	-0.01		Difference	-0.09

4. CONCLUSIONS

Rill erosion causes the fertile topsoil to drift by starting to flow from weak and loose areas in the soil due to precipitation or water accumulation. As a result, subsoil with a more compact structure emerges. In this study, a simple and cost-effective system is proposed to analyze the effects of rill erosion, frequently encountered in nature. System was realized with Kinect Sensor and Raspberry Pi in hardware and Python and MATLAB in software. Rill erosion effects of simulated various flow rates on soil types were analyzed. The soil volume lost due to rill erosion was calculated with the analyses made. By examining the depth images obtained, the displacement of the soil particles and the soil areas swelling with water were also visualized as soil loss. When the depth images obtained after the system created with the images obtained with the digital camera were examined, it was seen that the topography of rill erosion was revealed harmoniously. With the Kinect Sensor placed at the height of 70 cm,

volume changes of 1.3812 mm^3 could be detected as a unit. It has been observed that the system developed independently of soil types gives consistent results. It is considered that the system will be portable and low-cost to provide ease of use in the field. In future studies, this system will be easily integrated into remote measurement systems to monitor areas that may be exposed to rill erosion continuously.

Author Contribution Statements The authors contributed equally to this work.

Declaration of Competing Interests The authors declare that they have no known competing financial interests or personal relationships that could have appeared to influence the work reported in this paper.

References

[1] Rieke-Zapp, D. H., Nearing, M. A., Digital close range photogrammetry for measurement of soil erosion, *Photogramm. Rec.*, 20 (109) (2005), 69-87.

[2] Foldager, F. F., Pedersen, J. M., Skov, E. H., Evgrafova, A., Green, O., LiDAR-Based 3D scans of soil surfaces and furrows in two soil types, *Sensors*, 19 (3) (2019), 661, https://doi.org/10.3390/s19030661.

[3] Stefano, C. D., Palmeri, V., Pampalone, V., An automatic approach for rill network extraction to measure rill erosion by terrestrial and low-cost unmanned aerial vehicle photogrammetry, *Hydrol. Process.*, 33 (2019), 1883-1895, https://doi.org/10.1002/hyp.13444.

[4] Eitel, J. U. H., Williams, C. J., Vierling, L. A., Al-Hamdan, O. Z., Pierson, F. B., Suitability of terrestrial laser scanning for studying surface roughness effect on concentrated flow erosion processes in rangelands, *Catena*, 87 (3) (2011), 398-407, https://doi.org/10.1016/j.catena.2011.07.009.

[5] Li, P., Ucgul, M., Lee, S. H., Saunders, C., A new method to analyse the soil movement during tillage operations using a novel digital image processing algorithm, *Comput. Electron. Agric.*, 156 (2019), 43-50, https://doi.org/10.1016/j.compag.2018.11.009.

[6] Saygın, S. D., Süreç tabanlı modellemede parmak erozyonu toprak duyarlılığı parametresinin fiziksel olarak belirlenmesi, (2020). Program Kodu: 3001 Başlangıç AR-GE. Proje No: 1180111.

[7] Sharma, K., Kinect sensor based object feature estimation in depth images, *IJSIP*, 8 (12)

(2015), 237-246, http://dx.doi.org/10.14257/ijsip.2015.8.12.23.

[8] Mobini, A., Behzadipour, S., Foumani, M. S., Accuracy of kinect's skeleton tracking for upper body rehabilitation applications, *Disabil. Rehabilitation. Assist. Technol.*, 9 (4) (2013), 344-352, https://doi.org/10.3109/17483107.2013.805825.

[9] Pinto de Oliveira, H. F., An Affordable and Practical 3D Solution for the Aesthetic Evaluation of Breast Cancer Conservative Treatment, (2013). Ph.D. Thesis, Faculdade De Engenharia Da Universidade Do Porto, Programa Doutoral em Engenharia Electrotecnica e de Computadores, Porto.

[10] Mallick, T., Das, P. P., Majumdar, A. K., Characterizations of noise in kinect depth images: a review, *IEEE Sens. J.*, 14 (6) (2014), 1731-1740, https://doi.org/10.1109/JSEN.2014.2309987.

DESIGN AND IMPLEMENTATION OF A MICROCONTROLLER BASED SPLIT AIR CONDITIONER CONTROL SYSTEM

Oğuzhan TİMUR[1] and Ahmet TEKE[1]

[1]Electrical and Electronics Engineering, Çukurova University,
Adana, TURKEY

ABSTRACT. Different methods should be developed to work on energy efficiency in the electrical systems that do not allow outside intervention in the control part. In this study, the command and control of split air conditioners is carried out through hardware and software designed using the embedded system board. Infrared signals in the remote control device of the air conditioner were read with the developed circuit and recorded in the internal memory of the card, and these codes were used for energy efficiency studies. The obtained codes were used in 2 different applications. Thermal camera technology has been used instead of the traditional presence and motion sensors, which cannot achieve the desired success in asset detection in the absence of motion in the implemented applications. In this way, the presence of living things in the areas where the application is made has been detected with a much higher sensitivity regardless of the movement. As a result of the realized studies on the existing systems, 30% energy saving potential is determined approximately.

1. INTRODUCTION

Depending on the development of technology, the need for energy has also increased. The energy consumption of buildings, especially in cities, has risen dramatically in recent decades as a result of population growth, improved building services, and increasing levels of comfort [1]. In industrialized economies such as the Europe and the United States, buildings consume a significant amount of energy [2]. Buildings consume up to 31% of worldwide energy demand, 47.6% of total US energy consumption, and nearly 40% of total European energy consumption [3-5].

When the studies are reviewed in detail, it is seen that energy efficiency and saving studies focus on two different approaches as reducing energy consumption and using renewable energy sources [6]. With the effect of global warming, the demand for air conditioning devices has increased. Naturally, energy consumption and, accordingly, energy generation costs have also increased. Consequently, it has become a necessity to adopt high energy efficient air conditioners and to carry out energy efficiency studies in low efficiency air conditioners [7].

Air conditioners and electric fans used to keep an ambient cool are accounted for 20% of the total energy consumption in buildings. Due to the economic growth of the world, the living standards of human beings have increased. Due to the economic growth of the world, the living standards of human beings have increased. The increase in living standards will increase the rate of air conditioner usage and this trend will continue in the future due to global warming [8,10].

The purpose of air conditioning systems is to improve the air quality inside buildings in terms of temperature and humidity, as well as to provide a healthy and comfortable environment [11]. In the literature, it has been seen that researchers and manufacturers have started to pay more attention to thermal comfort [12,13].

A split air conditioner (SAC) consists of an indoor unit and an outdoor unit, including evaporator, compressor, condenser and capillary tube [14,15]. In some investigated sources, the capillary tube is named as an expansion valve. The main parts of a SAC have shown in Figure 1. SACs have a significant detrimental influence on global environmental pollution and energy consumption, despite the fact that it enhances human living conditions [16].
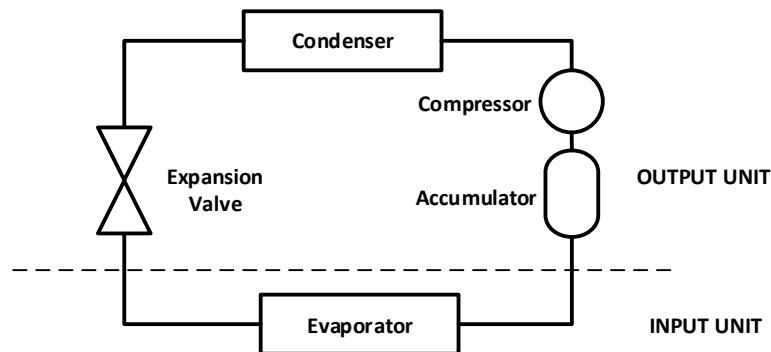

FIGURE 1. The main parts of a SAC.

The most energy consuming part of the air conditioner is the compressor. The most classical method used to reduce the energy consumption of the compressor is the use of an inverter. When the studies in the literature are scrutinize in detail, it is seen that most of the studies are related to compressor [17].

Researches show that speed control of the compressor motor usually has been carried out either using inverter or pulse width modulation (PWM) devices. While the designing of the PWM devices, microcontroller based embedded cards are preferred additional to PIC or other integrated circuits. Sometimes desired results could be obtained without the need for additional devices by simply using an embedded card. In [18], A microcontroller based PWM device has been designed by Podder and his friends to reduce the energy consumption of SAC. As a result of their studies, it has been determined that at least 50 percent savings can be made.

Many different methods are used in the energy saving studies of SAC. In [19], Harby and Amri provided that the air entering the air conditioner was pre-cooled before entering the air conditioner to perform energy saving in their experimental study. As a result of the pre-cooling, energy savings of up to 20% have been achieved. A similar study was carried out by Yang et al. in 2021. In this study, unlike the other study, condensate water was used to decrease the air flow temperature around the condenser of SAC. Depending on the operating mode of the SAC, energy savings were made at different rates. The maximum amount of savings achieved is around 20% [20]. In addition to these two studies, another similar study was performed by Atmaca and his friends. In this third study, evaporative cooled condenser was proposed. In this experimental study, the condenser in the outdoor unit is cooled by an evaporative pad with water circulation. As a result of this study, while the total electricity consumption reduced by up to approximately 12.4%, the total cooling capacity rose up to 18.6% [21].

Some air conditioners in schools, hospitals and similar public buildings continue to operate by leaving them on at noon, evening and even late at night. SACs which have left on after working hours consume unnecessary energy. Usually, the responsible personnel manually check whether the air conditioners are on or off. Consequently, some SACs remain open for a long time [22].

Most of the studies in the literature need to internal modification of the SACs. It means the intervention in the control unit and electronic parts of the SACs. In this proposed study, it is aimed to control the air conditioner using only remote control codes without interfering with the cards and control units of the air conditioner. Existing control codes are read by using IR receiver and saved in the internal memory of the embedded card and then with the helping of developed algorithm and these codes, SACs can be controlled without any intervention. Proposed study has been used in two different scenarios and determined to success realization of energy savings.

2. MATERIAL AND METHOD

2.1. Material

2.1.1. Design and implementation of SAC control system

2.1.1.1. **The controlling of SAC.** SACs have been controlled by IR (Infrared) remote controls. If desired to control by using computer instead of the remote controller, IR codes must be read firstly. After the codes is read and the saved, recorded codes must be send to the SAC with IR transmitter. Because of this, realized study consists of two parts mainly. First section is for receiving and second section is for transmitting. This implementation will be used for controlling of SACs. Realized study were written by using C# and ASP.Net. Desktop application was written by using C# in Microsoft Visual Studio. Web application was written by using ASP.NET in Microsoft Visual Studio. The main screen of C# and ASP.NET software has been shown in Figure 2. Although the two figures are similar in terms of appearance, the software codes and their components are different from each other.

2.1.1.2. **Case 1: The live checking implementation in empty room**. In this study, the time interval specified by the user, in room when presence detection the air conditioning switching off is to save energy via embedded system card. It has been

C# FORM DESIGN   **ASP.NET FORM DESIGN**
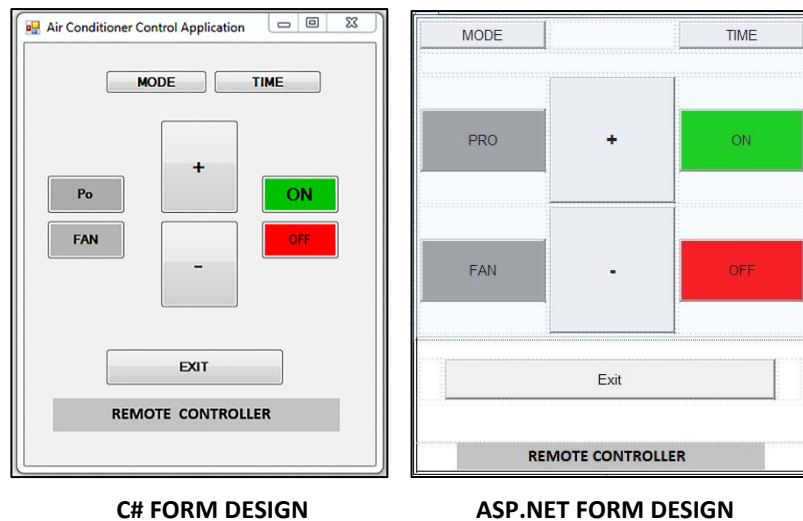
FIGURE 2. SAC remote controller form designs. C# form design (left); Asp.Net form design (right).
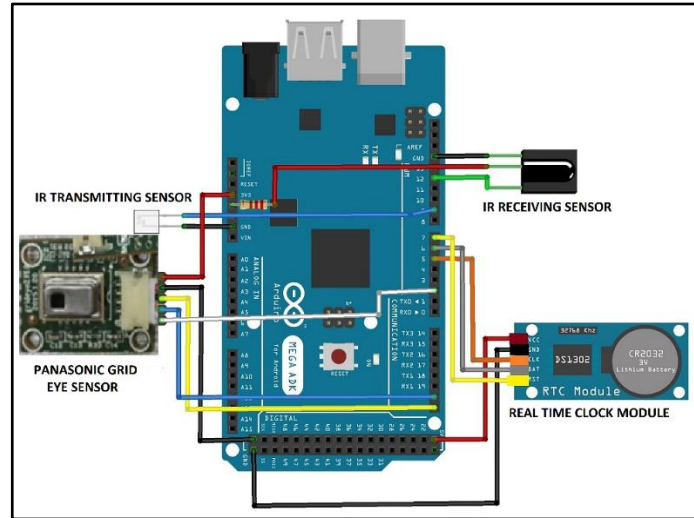
FIGURE 3. Empty room control circuit.

established using the Arduino Mega, fingerprint sensor, Panasonic Grid-Eye, IR receiver and transmitter sensor and the RTC module are used. Designed circuit is shown in Figure 3.

2.1.1.3. **Case 2: Energy saving implementation in air conditioners**. In the System Control Room (SCR) at a university hospital in Turkey, there are three SACs which have without any speed control devices. These SACs have been operated continuously for 7 days and 24 hours at the 22 ^{0}C temperature. Because SACs have not a speed control device, all of them work by STOP and START logic. In the realized study, conventional old SACs were operated such as SACs which have speed control devices. Whole SACs own the same trade mark and model. This situation provides some facilities such as the using of same IR code, management with same microcontroller. In addition to previous realized study, temperature sensor has been added in this study to measure ambience temperature and the grid eye sensor has been removed from the circuit because no asset detection is required.

2.2. **Method**

2.2.1. **Case 1: The live checking implementation in empty room.** In this circuit, Panasonic grid eye sensor was detected while a person is in the room or not. If the
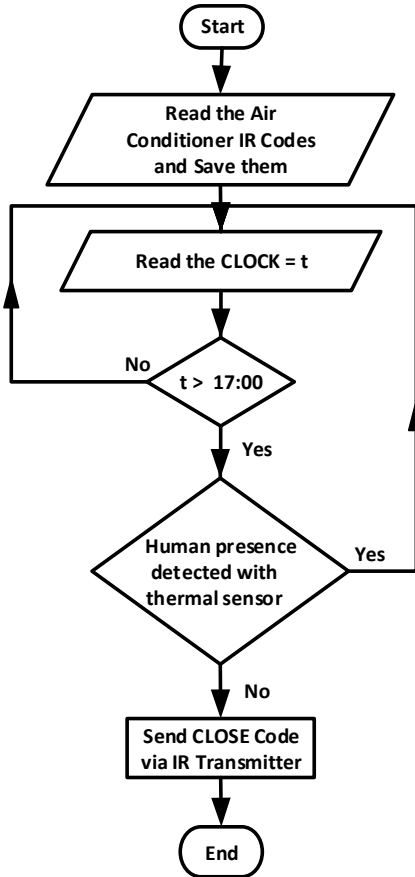
FIGURE 4. The algorithm flowchart of empty room control circuit.

room is empty and the time is after 5 p.m., SAC will be turned off automatically. The algorithm flowchart of the realized study has shown in Figure 4.

According to this algorithm, IR codes of SAC are read from the SAC remote controller and saved them primarily. After that, CLOSE command is sent after 17:00 pm if there is no the live in the room. Thus, after the working hours, open SACs will be automatically switched off.

In the realized study, printed wiring board has been designed as Arduino shield for the installation of used electronic devices. The designed printed wiring board figure has been shown in Figure 5. In addition, the picture of whole realized study is given in Figure 6.
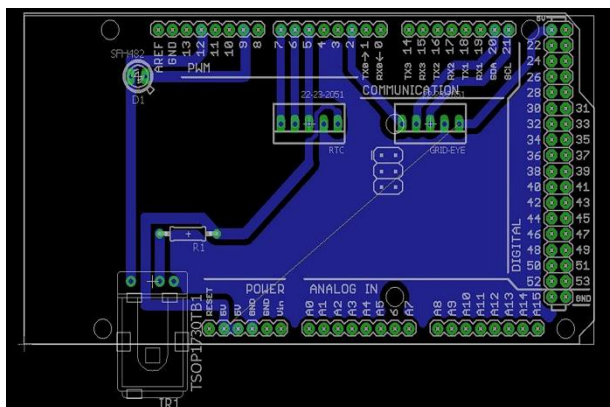
FIGURE 5. The printed wiring board of realized study.
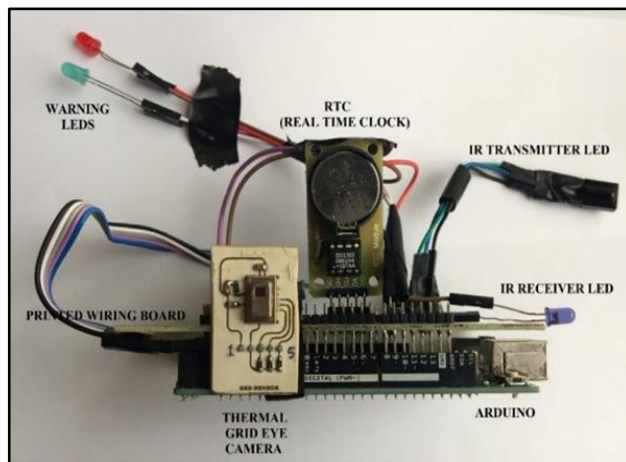
FIGURE 6. The picture of carried out empty room control circuit.

2.2.2. **Case 2: Energy saving implementation in air conditioners.** According to measured ambience temperature, SACs increase or decrease their own temperature value. Moreover, if all SACs do not need to work at the same time, SACs will be shut down respectively. If the SAC is needed to adjust the ambient temperature, the system will automatically activate the SAC as needed. Realized study is not only supported at the SACs in the existing SCR but also designed to manage the desired the numbers of SACs at the same time. The flowchart of carried out algorithm is shown in Figure 7.
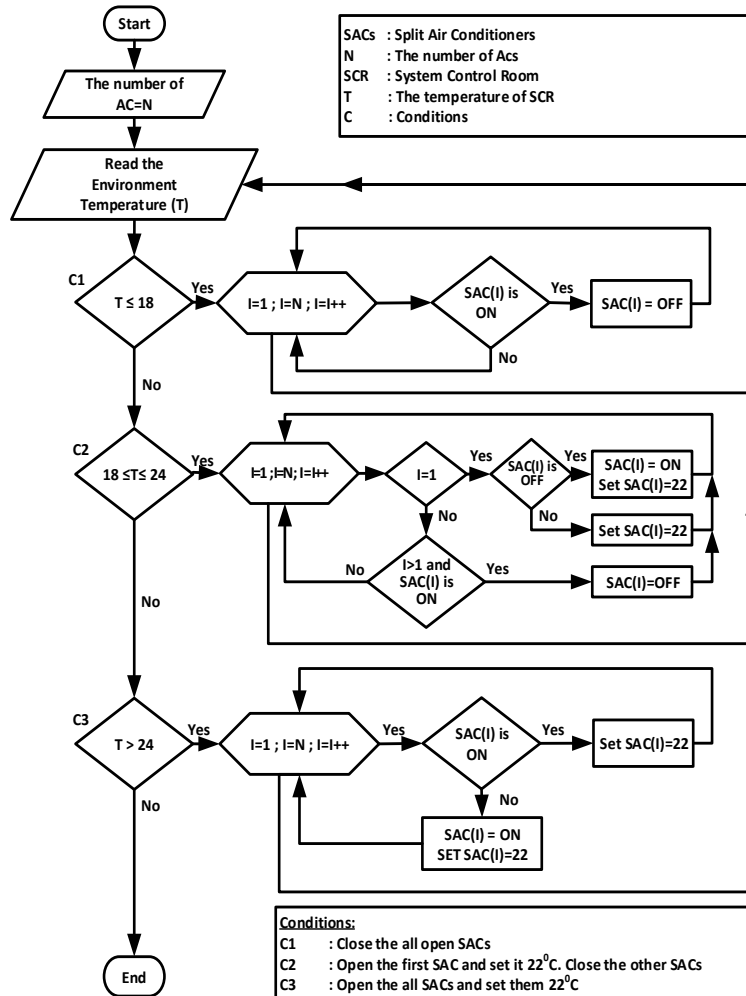
FIGURE 7. The flowchart algorithm of SACs management system.

The flowchart algorithm of the SAC management system can be summarized with the following steps.

1. Input the total number of air conditioners to be used (N)
2. Measure the ambient temperature (T)
3. C1: (Condition 1)
   If ambient temperature T is less or equal to 18^0C then, all the air conditioners are checked. Furthermore, the open ones will be turned off and when the loop ends it returns to reading the environment temperature level
4. C2: (Condition 2)

If the ambient temperature T is between 18^0C and 24^0C then all the air conditioners are checked. If the first air conditioner is turn off, it will turn on and set to 22^0C.The other air conditioners will be turned off if they are on and when the loop ends it returns to reading the environment temperature level

5. C3: (Condition 3)

   If the ambient temperature is greater than 24^0C then all the air conditioners are checked and the open ones will be set to 22^0C. If the air conditioner which is checked is off, it will be turned on and will be set to 22^0C and when the loop ends it returns to reading the environment temperature level.

3. RESULTS

Total energy consumption of existing SACs has been measured for a week. Later, SAC management system has been activated and same measurement, with the same software and the same smart plug, has been realized again. The studies were carried out in December. Energy consumption was measured by a low cost intelligent device (iDEV) which has %2 accuracy. iDEV was designed and implemented by Timur and his friends [23]. Total energy consumption of the whole SACs was measured as approximately 1,008 KWh. When the SAC management system is active, nearly 706 KWh total energy consumption for whole SACs were also measured. As a result of realized measurements, it was determined that approximately 30% energy saving was performed by using AIRCON management system. This means that one of the three SACs is working unnecessarily in December.

4. CONCLUSIONS

In this study, microcontroller-based hardware and software design has been carried out in order to achieve energy efficiency in split air conditioners. First of all, the codes of the control of the air conditioner to be worked on were read by the infrared receiver and recorded in the memory of the embedded card. These saved codes were sent to the split air conditioner with the infrared transmitter circuit, allowing the air conditioner to be controlled. Test applications were carried out on desktop and web-based using C# and ASP.NET platforms. Then the obtained codes were used in two different applications. In the first application, it was ensured that the air conditioners that were open outside of working hours were turned off when there was no one in the environment. In the second application, 3 split air conditioners working simultaneously in the system room were operated in a controlled manner in a sequential manner. Thus, devices that cause energy loss by being operated when not needed are prevented from throwing away energy (energy wasting). Although the

applications made save energy at different levels according to the months worked, the results obtained showed that at least 30% energy saving was achieved.

Author Contribution Statements Authors are equally contributed to the paper. All authors read and approved the final copy of the manuscript.

Declaration of Competing Interests The authors declare that they have no known competing financial interests or personal relationships that could have appeared to influence the work reported in this paper.

REFERENCES

[1] Perez-Lombard, L., Ortiz, J., Pout, C., A review on buildings energy consumption information, *Energy Build.*, 40 (2008), 394-398, https://doi.org/10.1016/j.enbuild.2007.03.007.

[2] Rashid, S. A., Haider, Z., Hossein. S. M. C., Memon, K., Panhwar, F., Mbogba, M. K., Hu, P., Zhao, G., Retrofitting low-cost heating ventilation and air-conditioning systems for energy management in buildings, *App. Energy,* 236 (2019), 648-66, https://doi.org/10.1016/j.apenergy.2018.12.020.

[3] Johansson, T. B., Patwardhan, A. P., Nakicenovic, N., Gomez-Echeverri L., Global Energy Assessment: Toward a Sustainable Future, Cambridge University Press, (2012).

[4] Agarwal, Y., Balaji, B., Gupta, R., Lyles, J., Wei, M., Weng, T., Occupancy-driven energy management for smart building automation, *Proceedings of the 2nd ACM Workshop on Embedded Sensing Systems for Energy-Efficiency in Building: ACM*, (2010), 1-6, https://doi.org/10.1145/1878431.1878433.

[5] Directives, Directive 2010/75/EU of the European Parliament and of the Council, *OJEU*, 334 (2010), 17-119.

[6] Ali, A. O., Elmarghany, M. R., Abdelsalam, M. M., Sabry, M. N., Hamed, A. M., Closed-loop home energy management system with renewable energy sources in a smart grid: a comprehensive review, *J. Energy Storage*, 50 (2022), 104609, https://doi.org/10.1016/j.est.2022.104609.

[7] Elsaid, A. M., A novel design, implementation and performance evaluation of the first electronic expansion ejector for energy saving of a mini split air conditioner controlled by inverter, *Energy Convers. Manag.*, 260 (2022), 115603, https://doi.org/10.1016/j.enconman.2022.115603.

[8] Tracking Sustainable Development Goal 7: The Energy Progress Report 2022. https://trackingsdg7.esmap.org/data/files/download-documents/sdg7-report2022-full_report.pdf.

[9] Santamouris, M., Cooling the buildings – past, present and future, Energy and Build., 128

(2016), 617-638, https://doi.org/10.1016/j.enbuild.2016.07.034.

[10] Ürge-Vorsatz, D., Cabeza, L. F., Serrano, S., Barreneche, C., Petrichenko, K., Heating and cooling energy trends and drivers in buildings, *Renew. Sustain. Energy Rev.*, 41 (2015), 85-98, https://doi.org/10.1016/j.rser.2014.08.039.

[11] Mohammed, J. A., Mohammed, F. M., Jabbar, M. A., Investigation of high performance split air conditioning system by using hybrid PID controller, *App. Therm. Eng.*, 129 (2018), 1240-1251, https://doi.org/10.1016/j.applthermaleng.2017.10.113.

[12] Shiming, D., Zheng, L., Minglu, Q., Indoor thermal comfort characteristics under the control of a direct expansion air conditioning unit having a variable-speed compressor and a supply air fan, *App. Therm. Eng*., 29 (2009), 2187-2193, https://doi.org/10.1016/j.applthermaleng.2008.10.011.

[13] Calvino, F., Gennusa, M. L., Morale, M., Rizzo, G., Scaccianoce, G., Comparing different control strategies for indoor thermal comfort aimed at the evaluation of the energy cost of quality of building, *App. Therm. Eng.*, 30 (2010), 2386-2395, https://doi.org/10.1016/j.applthermaleng.2010.06.008.

[14] Che, Y., Yang, J., Zhou, Y., Zhao, Y., He, W., Wu, J., Demand response from the control of aggregated inverter air conditioners, *IEEE Access*, 7 (2019), 88163-88173, https://doi.org/10.1109/ACCESS.2019.2925659.

[15] Wu, Z., Li, N., Wargocki, P., Peng, J., Li, J., Cui, H., Field study on thermal comfort and energy saving potential in 11 split air conditioned office buildings in Changsha, China, *Energy*, 182 (2019), 471-482, https://doi.org/10.1016/j.energy.2019.05.204.

[16] Hui, H., Ding, Y., Zheng, M., Equivalent modeling of inverter air conditioners for providing frequency regulation service, *IEEE Trans. Ind. Electron.*, 66 (2) (2019), 1413-1423, https://doi.org/10.1109/TIE.2018.2831192.

[17] Wei-Han, C., Huai-En, M., and Tun-Ping, T., Performance improvement of a split air conditioner by using an energy saving device, *Energy Build.*, 174 (2018), 380-387, https://doi.org/10.1016/j.enbuild.2018.06.055.

[18] Podder, P., Debnath, T., Faruk, O., Islam, S., A Microcontroller based efficient scheduling system for air conditioner focusing on maximum electricity savings using PWM concept, *IJATCSE*, 10 (2) (2021), 1183-1192, https://doi.org/10.30534/ijatcse/2021/1001022021.

[19] Harby, K., Amri, F. A., An investigation on energy savings of a split air-conditioning using different commercial cooling pad thicknesses and climatic conditions, *Energy*, 182 (2019), 321-336, https://doi.org/10.1016/j.energy.2019.06.031.

[20] Yang, H., Pei, N., Liu, L., Fan, M., Qin, Y., Experimental study on the effect of condensate water on the performance of split air conditioning system, *Energy Rep.*, 7 (2021), 840-851, https://doi.org/10.1016/j.egyr.2021.01.037.

[21] Atmaca, I., Senol, A., Caglar, A., Performans testing and optimization of split type air conditioner with evaporately-cooled condenser, *Eng. Sci. Technol. Int. J.,* 32 (2022),

101064, https://doi.org/10.1016/j.jestch.2021.09.010.

[22] Yu, K., Cao, Z., Liu. Y., Research on the optimization control of the central air-conditioning system in university classroom buildings based on TRNSYS software, *10th International Symposium on Heating, Ventilation and Air Conditioning, ISHVAC2017*, *Procedia Eng.,* 205 (2017), 1564-1569, https://doi.org/10.1016/j.proeng.2017.10.261.

[23] Timur, O., Zor, K., Celik, O., Teke, A., Enhancement of a low-cost intelligent device for improving energy efficiency in buildings, *Commun. Fac. Sci. Univ. Ank. Series A2-A3*, 60 (2) (2018), 103-128, https://doi.org/10.1501/commua1-2_0000000118.

A METHOD FOR ANALYZING SUSPECT-FILLER SIMILARITY USING CONVOLUTIONAL NEURAL NETWORKS

Dervis Emre AYDIN[1] and Yilmaz AR[2]

[1]Lawyer, Ankara Bar, Ankara, TURKEY
[2]Department of Computer Engineering, Ankara University,
Ankara, TURKEY

ABSTRACT. Eyewitness misidentifications are one of the leading factors in wrongful convictions. This study focuses on the structure of the lineups, which is one of the factors that cause misidentification, and the use of artificial intelligence (AI) technologies in the selection of fillers to be included in the lineups. In the study, AI-based face recognition systems are used to determine the level of similarity of fillers to the suspect. Using two different face recognition models with a Convolutional Neural Network (CNN) structure, similarity threshold values close to human performance were calculated (VGG Face and Cosine similarity = 0.383, FaceNet and Euclidean l2 = 1.16). In the second part of the study, the problems that are likely to be caused by facial recognition systems used in the selection of fillers are examined. The results of the study reveal that models responsible for facial recognition may not suffice alone in the selection of fillers and, an advanced structure using CNN models trained to recognize other attributes (race, gender, age, etc.) associated with similarity along with face recognition models would produce more accurate results. In the last part of the study, a Line-up application that can analyze attributes such as facial similarity, race, gender, age, and facial expression, is introduced.

1. INTRODUCTION

Extensive research on wrongful convictions reveals that misidentifications of eyewitnesses are leading factors that cause errors [1-4]. Like legal experts, scientists are aware of this problem. For decades, scientists have been working to develop more appropriate identification procedures to determine the factors that cause

misidentification and to minimize the risks that may arise when collecting eyewitness evidence [5].

Eyewitness experts examine factors affecting eyewitness identifications under two main groups: System variables and estimator variables [6]. Crime and eyewitness-related factors such as stress, violent content of the crime, exposure time, and perpetrator characteristics are called estimator variables [7-12]. The factors under the control of the justice system and related to the accuracy of the identification are covered under the heading of system variables [13]. Identification methods [14], police interrogation tactics [15], feedback [16], and post-event information [17] are the main areas of study on system variables.

Identification procedures are also one of the system variables affecting eyewitness identifications [18]. There are many factors related to the accuracy of the identification, such as the way the lineup is shown (live or photographed; sequential or simultaneous), the number of fillers, witness instructions, and eyewitness confidence [13, 19, 20]. One of these factors is the criteria for the selection of fillers to be included in the lineups [21].

In 1998, as a result of The Executive Committee of the American Psychology-Law Society of the APA, recommendations based on scientific findings on how to collect eyewitness evidence were published under four headings [22]. A new study has recently been published, including five new recommendations in addition to the four recommendations from the previous study [13]. This recent study explored selecting fillers for lineups under the fourth recommendation [13].

Wells et al. (2020) suggest that "there should be only one suspect per lineup and the lineup should contain at least five appropriate fillers who do not make the suspect stand out in the lineup based upon physical appearances or other contextual factors such as clothing or background". Two main approaches are discussed on the similarity of fillers in the last study [13].

1.1. Filler Search Approaches

1.1.1. **Match-to-description.** The first approach, called match-to-description, takes into account only the characteristics of the eyewitness in the description when selecting fillers [23]. It is assumed that this approach prevents possible misidentification due to the match of the fillers in the lineup with the description of the culprit, and facilitates the recognition of the perpetrator thanks to the variety in the facial shapes of the members of the lineup [21].

1.1.2. **Match-to-appearance.** In the other approach called match-to-appearance or resemble-suspect, the fillers are selected among those that physically resemble the suspect while creating a lineup [23]. There is a lot of research showing that innocent

suspects are more likely to be misidentified in lineups created with fillers with a low likeness to suspects [24]. At the same time, a study examining eyewitness identification procedures around the world suggests that the match-to-appearance approach is much more widely used [25]. However, there is also some criticism of this approach.

The most important criticism of the resemble-suspect approach is that it has no criterion or "stopping point" for determining how similar the fillers should be [21, 13]. When the lineup is created with fillers very similar to the suspect, it will be very difficult to identify the perpetrator from within the lineup [13]. The opinion of experts who advocate the match-to-description approach is that this approach does not include such a risk due to its natural stopping point (the witness' description of the culprit) [21].

Although large-scale studies comparing the two approaches have highlighted findings supporting the match-to-description approach [24, 26] experts say the match-to-description approach should only be used when a complete description is obtained [13]. In cases where no exact description is taken or when the description of the eyewitness and the possible suspect are inconsistent with some physical characteristics, the selection of fillers that match the current appearance of the suspect stands out as a generally accepted hybrid approach [13].

The current recommendation from the U.S. Department of Justice on the similarity criterion includes a hybrid approach:

"3.2. Filler should generally fit the witness's description of the perpetrator, including such characteristics as gender, race, skin color, facial hair, age, and distinctive physical features. They should be sufficiently similar so that a suspect's photograph does not stand out, but not so similar that a person who knew the suspect would find it difficult to distinguish him or her. When viewed as a whole, the array should not point to or suggest the suspect to the witness [27]".

According to Wells et al., most research on suspect-filler similarity is based on subjective similarity criteria. Therefore, they noted that the appropriate level of suspect-filler similarity remains a question that science has not yet answered [13]. Based on this problem, we aimed to use AI-based facial recognition technologies to detect the appropriate level of similarity in suspect-filler similarity. First, we reviewed the computer-based systems already used when preparing the lineups.

1.2. **Computer-Based Systems Used in the Selection of Fillers**

1.2.1. **Match-to-description based systems.** Several studies show that computer systems are used by many police departments in the U.S. to access photo databases (driver's license and criminal photos) to create lineups [28-30] Officers have access to filler photos with desired characteristics by entering suspect's physical

characteristics (race, gender, hair color, etc.) [29]. The VIPER (Video Identification Parade Electronic Recording) system used in the United Kingdom is also a filler database based on the match-to-description approach [31].

1.2.2. **Match-to-appearance / resemble-suspect based systems.**

Tredoux's Euclidean Approach. We see that Tredoux (2002) was the first researcher to use a statistically based suspect-filler similarity approach in the selection of fillers, and he used the euclidean distance between two faces as a similarity criterion based on Valentine's (1991) multidimensional 'face space' system [23, 32, 33]. In Valentine's (1991) multidimensional face space, the similarity between human faces is rated as multidimensional features such as race, age, gender, face shape, eye size, etc. This system, called multidimensional scaling, calculates the similarity between faces using the ratings of multiple features [34].

We have not been able to find any information on whether this approach used by Tredoux (2002) in the selection of fillers is utilized in real-life and field research. But there has been research in recent years showing that face recognition software has been used to select fillers from large photo databases [28].

2. Face Recognition Systems

In recent years, we have seen facial recognition systems widely used in areas such as video surveillance, identification, and autonomous vehicles. There are various techniques in face recognition that focus on the features of certain elements of the human face or use the entire face or use these approaches in a hybrid way [35]. It is possible to classify these approaches used in facial recognition as feature-based and image-based approaches [36].

Feature-based Approaches: The feature-based approach is based on data on the facial features such as eyes, eyebrows, and noses on the face and the intensity of these features [37]. It is thought that the most distinctive elements in the face area are the forehead and eye area [38].

Image-based Approaches: In image-based approaches used in facial recognition systems, artificial neural networks are widely used [36]. Artificial neural networks are one of the subfields in machine learning, a subset of artificial intelligence [39]. In the image-based approach based on artificial neural networks, techniques from statistical analysis and machine learning are utilized to find facial characteristics [36]. The face recognition models in the Deepface framework that we used in our study are also Convolutional Neural Networks-based face recognition models, a subtype of artificial neural network structure [40].

Convolutional Neural Networks: Convolutional Neural Networks (CNN) is a kind of deep learning model inspired by the working structure of the animal visual

cortex [41]. It is also preferred for tasks such as face recognition and gender classification due to its common use in computer vision tasks such as image classification and object recognition [42]. In a CNN structure, the input image is processed on layers with different tasks, and a vector output is obtained as a result [43].

The most important layer of a basic CNN structure is the Convolutional Layer, which consists of convolutional filters. The input image is filtered with convolutional filters of different sizes and feature maps are created. The pooling layer is used to create a subsampling of the feature maps. The activation function (non-linearity) used to match the input is a basic function in neural network structures and decides whether or not a neuron is fired by referring to a specific entry. The Fully-Connected Layer, which is usually found at the end of CNN structures, is responsible for the classification [39].

3. THE CURRENT STUDY

Although it is thought that face recognition software may be more objective than face recognition by humans due to their mathematical algorithm-based ratings [34], research by Bergold and Heaton (2018) shows that there are some risks. The results of the study using a face recognition software named Betaface (Demo) by Bergold and Heaton (2018) where they studied the effect of the facial image database size on the accuracy of the identification showed that identification decreased when the fillers were selected from the large face database [28]. Moreover, there is concern that this situation may pose a serious problem as the use of these systems becomes more common [13]. In our opinion, it seems possible to detect an objective "stopping point" by using facial recognition software in order to overcome this problem of over-similarity.

In our research, we first focused on detecting an objective similarity rate that would be used in suspect-filler similarity using an AI-based face recognition model. For this purpose, we used the VGG Face and FaceNet facial recognition models included in the Deepface framework. We determined a stopping threshold value where the performance of the models is closest to the human performance. Then we created a list of potential fillers using Betaface (demo) software. With this sample list, we've explored possible problems with facial recognition systems. Finally, we have developed an open-source AI-based application that analyzes the suspect filler similarity.

3.1. **Method and Material**

3.1.1.   **Deepface framework and facial recognition models.**

Deepface Framework. Deepface is an open-source facial recognition package released with an MIT license developed for the Python programming language [40]. We used the Deepface package in our study as it is able to perform the four common steps (face detection, alignment, vector representation, and verification) in modern facial recognition systems in a practical way. The framework includes Convolutional Neural Networks (CNN) based facial recognition models such as VGG-Face, Google FaceNet, OpenFace, and Facebook DeepFace [44, 40].

VGG Face Facial Recognition Model. One of the facial recognition models we used in our study was the VGG Face facial recognition model, which is the default model in the Deepface framework. Developed by the Visual Geometry Group at the University of Oxford, VGG-Face is a CNN model with 22 layers and 37 deep units. The image size of the model's input layer is 224x224x3, producing a feature vector of 2622 at the end of the process. The accuracy performance of the model in the LFW data set [45] was 98.78% [46]. Human performance in the LFW data set was found to be 97.5% [47, 43].

FaceNet Facial Recognition Model. The second facial recognition model used in our study is FaceNet face recognition model, which is also included in the Deepface package. FaceNet, developed by Google, is a CNN model of 140 million parameters. FaceNet produces a 128-dimensional feature vector from the face image it receives as inputs of 160 x 160 x 3 dimensions [48]. The accuracy performance of the model in the LFW data set [45] was 99.63% [46].

3.1.2. **Metrics.** CNN-based face recognition models are responsible for producing feature vectors that best express the face images they receive as inputs. The similarity between the two faces is measured by the distance between the vectors. Different metrics such as Cosine Similarity, Euclidean Distance and Euclidean L2 are used when calculating the distance between vectors [40]. As the similarity between the two face images increases, the calculated distance value decreases, while the distance value increases as the similarity decrease. A threshold value must be determined to decide whether the images belong to the same person [40].

In this way, it can be concluded that the images belong to the same person in cases where the distance between the vectors is below the threshold value. The threshold value to be used for this purpose is not a fixed value and should be determined separately according to different metrics for each facial recognition model.

The threshold value of the VGG Face model in the cosine metric by Serengil was calculated as 0.3751 through the statistical approach [49]. It is also seen that the threshold value in the cosine metric of the VGG Face model is calculated as 0.3147 through the decision tree-based C.4.5 algorithm, and the threshold value of the

FaceNet model in the Euclidean l2 metric is calculated as 0.90 through the decision tree-based C.4.5 algorithm [40].

The equations for the evaluation metrics precision, recall, F1-score and accuracy are given as follows:
Precision = TP / (TP + FP)
Recall = TP / (TP + FN)
F1-Score = 2 * (Precision * Recall) / (Precision + Recall)
Accuracy = (TN + TP) / (TN + TP + FN + FP)
(TP: True Positive, FP: False Positive, TN: True Negative, FN: False Negative)

3.1.3. **Our Datasets.** Some research on facial recognition systems reveals that the systems are more successful in males than females; they also produce more successful results in light-skinned people than in dark-skinned people [42]. Since we don't want this issue to cause a bias, which is important when determining the threshold value, we have created two separate datasets with face images. The first dataset, comprising a total of 48 images, includes four photographs of six female (2 Black, 2 White, and 2 Asian) and six male (2 Black, 2 White, and 2 Asian) celebrities. In the second dataset, there are four photographs of twelve different Black female celebrities. Since factors such as the quality of face images and the ratio of light affect the results [50], datasets were compiled from images with similar quality and light intensity.

4. Results

All the calculations in our study were performed using the Jupyter Notebook development environment through Python 3.9 programming language on a computer with Intel(R) Core(TM) i5-4300U CPU @ 1.90GHz 2.49 GHz processor and 8.00 GB Ram hardware power. VGG Face and FaceNet facial recognition models included in the Deepface framework were used to calculate the distance values between face images.

4.1. Calculation of the Threshold Value We Use in Our Method

4.1.1. **VGG face and cosine similarity.** In order to determine the first threshold value we used in our model, we first pre-labeled the facial images in the data sets we prepared according to whether they belonged to the same person. Then, using the *verify()* function in the Deepface package, we calculated the distance between the vector values of the facial images calculated by the VGG Face model according to the cosine metric. In this way, we have determined the distance values between faces

belonging to different people (False Positive) and distance values between faces belonging to the same people (True Positive) (Table 1).

TABLE 1. Datasets outcomes (VGG Face, Cosine Similarity).

Decision Context	Mixed Dataset		Black Women Dataset	
	False Positive	*True Positive*	*False Positive*	*True Positive*
N	1056	72	1056	72
Distance Mean	0.6576	0.1863	0.4833	0.1754
Distance SD	0.1284	0.61	0.0975	0.0649

Note. The results were calculated with Deepface Framework on Jupyter Notebook. Calculations were repeated 3 times until the constant value was received. Minor changes in values (0.015) can be observed based on the system's hardware performance.

Since we will use distance values between faces belonging to the same people when calculating the threshold value, we studied whether there is a statistically significant difference between the two groups in terms of this parameter. After we found that the groups confirm the normality assumption of True Positive distance values [51], we used the Independent Sample t-Test to analyze whether there was a significant difference between the groups (Table 2).

TABLE 2. Result of analysis black women dataset with mixed dataset (VGG Face, Cosine Similarity).

	Mixed Dataset		Black Women Dataset		t(142)	*p*	Cohen's *d*
Parameters	*M*	*SD*	*M*	*SD*			
True Positive Dist.*	0.186	0.061	0.175	0.064	1.041	0.30	0.063

Note. *Distance values between faces belonging to the same person.

As a result of the analysis, we found that there was no statistically significant difference between the datasets (M=0.186, SD=0.061), which had a balanced distribution in terms of gender and race, and the true positive distance values of the data set (M=0.175, SD=0.064) consisting solely of Black female celebrities (t(142)=1.041, p=0.30). Therefore, we continued our study with the findings of the Mixed dataset. In the next stage, we calculated the potential threshold values based on the statistical approach used by Serengil to calculate the threshold value (Threshold Value = True Positive Mean + Sigma * True Positive Standard Deviation) (Table 3). When we set the threshold value of 0.3693 (3σ), we found that

the model performed with 98.31 % accuracy. When we used 0.199 and 0.383 as the threshold value, we found that the model had the closest accuracy performance to human performance (97.5%) in the LFW data set (Table 3).

TABLE 3. Mixed dataset threshold values (VGG Face, Cosine Similarity).

Parameters	Mixed Dataset Outcomes				
		σ	2σ	3σ	
Distance	0.199*	0 .2473	0.3083	0.3693	0.383*
Precision	100.0%	100.0 %	100.0 %	79.12 %	72.0 %
Recall	61.11 %	83.33 %	97.22 %	100.0 %	100.0 %
F1 score	75.86 %	90.90 %	98.59 %	88.34 %	83.72 %
Accuracy	97.5% (Human)	98.93 %	99.82 %	98.31 %	97.5% (Human)

Note. The results were calculated with Deepface Framework on Jupyter Notebook. 1 sigma corresponds to 68.27% confidence, 2 sigma corresponds to 95.45% confidence, and 3 sigma corresponds to 99.73% confidence. * When we set the threshold at 0.199 and 0.383, the facial recognition system performs closest to human performance (97.5%) in the LFW dataset.

TABLE 4. Black women dataset threshold values (VGG Face, Cosine Similarity).

Parameters	Black Women Dataset Outcomes				
		σ	2σ	3σ	
Distance	0.199	0.2403	0.3083	0.3693	0.383
Precision	98.07 %	95.08 %	67.64 %	33.02 %	28.57 %
Recall	70.83 %	80.55 %	95.83 %	100.0 %	100.0 %
F1 score	82.25 %	87.21 %	79.31 %	49.65 %	44.44 %
Accuracy	98.04 %	98.49 %	96.80 %	87.05%	84.04 %

Note. The results were calculated with Deepface Framework on Jupyter Notebook.

4.1.2. **FaceNet and Euclidean L2.** We used the same method to determine the appropriate threshold value in the FaceNet model and the Euclidean L2 metric. Using the *verify()* function in the Deepface framework, we calculated the distance between the vector values of face images calculated by the FaceNet model according to the Euclidean metric (Table 5).

TABLE 5. Datasets outcomes (FaceNet, Euclidean L2).

	Mixed Dataset		**Black Women Dataset**	
Decision Context	*False Positive*	*True Positive*	*False Positive*	*True Positive*
N	1056	72	1056	72
Distance Mean	0.3722	0.6354	1.221	0.6087
Distance SD	0.0948	0.1015	0.1335	0.1262

Note. The results were calculated with Deepface Framework on Jupyter Notebook.

After finding that the true positive distance values of the images in mixed and Black women datasets confirm the assumption of normality according to the Kolmogorov-Smirnov Test, we used the Independent Sample t-Test to analyze whether there was a statistically significant difference between the groups (Table 6).

TABLE 6. Result of analysis black women data set with mixed data set (FaceNet, Euclidean L2).

	Mixed Dataset		**Black Women Dataset**		t(142)	*p*	Cohen's *d*
Parameters	*M*	*SD*	*M*	*SD*			
True Positive Dist.*	0.635	0.101	0.609	0.127	1.398	0.164	0.114

Note. *Distance values between faces belonging to the same person (TPD). M = It is the mean of the TPD values within the group. SD= It is the standard deviation of the TPD values within the group.

As a result of the analysis, we found that there was no statistically significant difference between the datasets (M=0.635, SD=0.101) with a balanced distribution in terms of gender and race and the true positive distance values of the data set (M=0.609, SD=0.127) consisting solely of Black female celebrities (t(142)=1.398, p=0.164). Therefore, we continued our study with the findings of the Mixed dataset. When we set the threshold value of 0.9399 (3σ) in the conditions in which we used the FaceNet facial recognition model and the Euclidean l2 metric, we found that the

model performed with 99.73% accuracy. When we used 0.68 and 1.16 as the threshold value, we found that the model had the closest accuracy performance to human performance (Table 7).

TABLE 7. Mixed dataset threshold values (FaceNet, Euclidean L2).

Parameters	Mixed Data Set Outcomes				
		σ	2σ	3σ	
Distance	0.68*	0.7369	0.8384	0.9399	1.16*
Precision	100.0 %	100.0 %	100.0 %	96.0 %	72.0 %
Recall	63.88 %	86.11 %	100.0 %	100.0 %	100.0 %
F1 score	77.96 %	92.53 %	100.0 %	97.95 %	84.21 %
Accuracy	97.69 %	99.11 %	100.0 %	99.73 %	97.60 %

Note. The results were calculated with Deepface Framework on Jupyter Notebook. 1 sigma corresponds to 68.27% confidence, 2 sigma corresponds to 95.45% confidence, and 3 sigma corresponds to 99.73% confidence. *When we set the threshold at 0.68 and 1.16, the facial recognition system performs closest to human performance in the LFW dataset.

TABLE 8. Black female dataset threshold values (FaceNet, Euclidean L2).

Parameters	Black Women Data Set					
		σ	2σ		3σ	
Distance	0.68	0.7349	0.8611	0.955*	0.9873	1.16
Precision	100.0%	100.0%	94.52 %	72.72%	58.53 %	17.69%
Recall	72.22 %	83.33 %	95.83 %	100.0%	100.0 %	100.0 %
F1 score	83.87 %	90.90 %	95.17 %	84.21%	73.84 %	30.06 %
Accuracy	98.22%	98.93 %	99.37 %	97.60%	95.47 %	70.30%

Note. The results were calculated with Deepface Framework on Jupyter Notebook. * When we set the threshold at 0.955, the facial recognition system performs closest to human performance in the LFW dataset.

4.2. **Similarity Results of Potential Fillers Listed with Betaface (demo).** In the second part of our study, we used facial recognition software called Betaface (demo) to create a sample fillers list. Betaface (demo) is a feature-based facial recognition system [34] that calculates over 22 and 101 points on the face [52].

Bergold and Heaton (2018) selected the top 12 people who most resembled the suspect from the database they created with facial recognition software called Betaface (demo). Then, with an experienced homicide detective selecting five people from 12 photographs, lineups were created to be used in the research. We also used software called Betaface (demo) to identify the top 10 people who most resembled the corresponding author of this article from within the celebrities' database (40000+ faces of famous people). We then calculated the vector distances of these 10 people according to the Cosine metric of the VGG Face model and the Euclidean L2 metric of the FaceNet model (Tables 9 and 10).

TABLE 9. Betaface (Demo) test (1-5).

Similarity Parametres	BetaFace (Demo) Images				
	1st	2nd	3rd	4th	5th
Betaface Similarity	83.3%	79.9%	79.7%	79.6%	78.7%
VGG-Face (Cosine)*	0.3094	0.3310	0.2386	0.3520	0.2422
FaceNet (EuclideanL2)*	0.9104	1.0300	1.0217	1.0686	0.9236

Note. *The results were calculated with Deepface Framework on Jupyter Notebook.

TABLE 10. Betaface (Demo) test (6-10).

Similarity Parametres	BetaFace (Demo) Images				
	6th	7th	8th	9th	10th
Betaface Similarity	78.3%	78.3%	77.6%	77.6%	77.1%
VGG-Face (Cosine)*	0.2171	0.2644	0.3717	0.4461	0.4448
FaceNet (EuclideanL2)*	1.0231	0.9693	1.1876	1.1519	1.1658

Note. *The results were calculated with Deepface Framework on Jupyter Notebook.

5. Discussion

5.1. **Appropriate Threshold Value.** In our research, we first focused on detecting an optimal level of similarity of fillers to the suspect that could be used as a stopping point. One of the problems that we encountered at this stage was that the facial recognition models we used had a higher accuracy performance than human performance (In Mixed data set (3σ): VGG Face = 98.31%, FaceNet = 99.73% (Table 3.7), in LFW data set: VGG Face = 98.95% FaceNet = 99.63% [46]). There is a risk that a system with a higher accuracy rate than humans is listing fillers who are difficult to distinguish by humans. Therefore, we preferred a system that has a similar accuracy performance to that of humans (97.5%).

5.1.1. Appropriate Threshold Value in VGG Face and Cosine Metric We found that the VGG Face facial recognition model performed 98.31% accuracy under a threshold of 0.3693 (3σ). When we set the threshold at 0.199 and 0.383, we found that the system was approaching the human performance level of 97.5% accuracy (Table 3). We decided to use 0.383 (sigma > 3) because the value 0.199 (sigma < 1) is not statistically secure enough. In this way, we tried to minimize the risk of people being included in the lineup, who cannot be distinguished by eyewitnesses because they are so similar. As a result, we decided that the optimal level of similarity (as a stopping point) that should be used in terms of suspect-filler similarity should be 0.383 under the condition that the VGG Face facial recognition model and cosine similarity metric are used.

5.1.2. **Appropriate threshold value in faceNet and Euclidean L2 metric.** We found that the FaceNet facial recognition model performed with 99.73% accuracy under a threshold of 0.3693 (3σ). When we set the threshold at 0.68 and 1.16, we found that the system was approaching the human performance level of 97.5% accuracy (Table 7). We decided to use 1.16 (sigma > 3) because the value of 0.68 (sigma < 1) is not statistically secure enough. In this way, we tried to minimize the risk of people being included in the lineup, who cannot be distinguished by eyewitnesses because they are so similar. As a result, we decided that the optimal level of similarity (as a stopping point) that should be used in terms of suspect-filler similarity should be 0.383 under the condition that the FaceNet face recognition model and Euclidean l2 metric are used.

5.2. **Risks in Selecting Fillers with Facial Recognition Software**

5.2.1. **Too much facial similarity.** In the second part of our study, we used Betaface (demo) software to list the top 10 results that resemble the corresponding author of this article from the celebrities' database. The similarity results calculated with

Betaface (demo), VGG Face, and FaceNet can be seen in Tables 9 and 10. We used the threshold values we identified at the previous stage to assess whether the 10 listed people were eligible to be included in the lineup in terms of their similarity to the suspect. When we used the threshold value of 0.383, which we set for VGG Face and cosine metric, we concluded that 8 out of 10 people listed by Betaface (demo) software were too similar to be used in the lineup. In the case where we used the threshold value of 1.16, which we set for FaceNet and Euclidean l2 metric, we concluded that 8 out of 10 people were too similar to be used in the lineup (Table 9-10). The results at this stage also supported the concern expressed by Wells et al. (2020) that facial recognition software would choose more similar fillers to the suspect if there was no stopping point.

5.2.2. **Other similarity factors.** Apart from facial geometry-based similarity, there are other factors to consider in the selection of fillers. Factors such as race, skin color, age, gender, eye color, hair color, hairstyle, facial hair, distinctive physical features, and photo background are some of the other factors to consider when creating a lineup [27,13]. In this second part of our study, we noticed that some of the people listed by Betaface (demo) software had discrepancies in skin color, and one had a long beard. However, we found that the result of facial similarity of these problematic samples remained below the threshold values that we set as a stopping point in both face recognition models. This is not surprising, especially given the verification-oriented working structure of CNN-based face recognition models, but it is also an indication that they alone will not be sufficient to create a lineup in terms of other factors associated with similarity. However, we also know that models using CNN structure can be trained in the classification of such features [40]. Therefore, we have concluded that an advanced structure created with other feature-based trained models together with the facial recognition model will allow for the use of both match-to-description and match-to-appearance approaches based on common and objective criteria.

5.3. **The Line-up Application.** The results of our study in the second part showed that models responsible only for facial recognition may not be sufficient in the selection of fillers. Therefore, we concluded that an advanced structure using CNN models trained to recognize other characteristics (race, gender, age, etc.) associated with similarity along with facial recognition models would produce more accurate results. Based on this result, we developed open-source software that can be analyzed based on factors such as facial similarity, race, gender, age, and facial expression (Figure 1, Note. The photos were created by https://generated.photos/ and do not belong to real people).
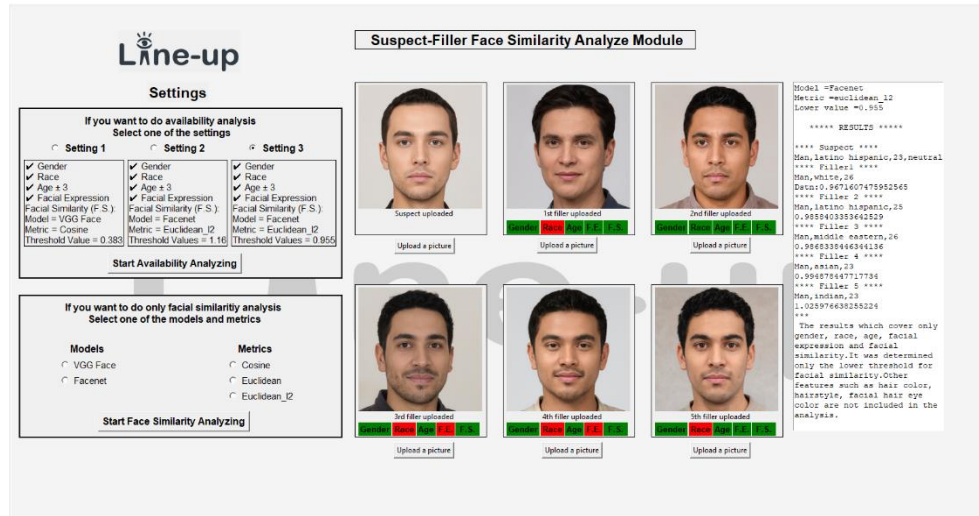
FIGURE 1. Line-up app.

We used the Python programming language and fully open-source software libraries, especially the Deepface framework when developing the Line-up application. The app allows users to perform suspect-filler similarity analysis by selecting one of the VGG Face and FaceNet facial recognition models and one of the cosines, Euclidean, and Euclidean l2 metrics according to their request. In cases where one of the default settings is selected or the appropriate threshold value range is determined, the face similarity eligibility results of the fillers uploaded to the system are listed. At the same time, conformity analysis of other similarity-related characteristics such as race, age, gender, and facial expression can be performed. With future developments, we aim to analyze other factors that will affect eyewitness identification, such as the eye color, hair color, hairstyle, facial hair, and photo background of the fillers.

6.   LIMITATIONS

6.1. **Performance Differences of Face Recognition Models**

6.1.1. **Demographic Challenges.** There are many reservations about the use of artificial intelligence-based facial recognition systems in public areas. One of the most commonly cited ethical issues is the risk of increasing social bias due to the change in system performance according to gender and skin color [42]. Research by Buolamwini (2017) shows that darker-skinned females are 32 times more likely to be misclassified than men with lighter skin. It has been concluded that this resulting bias is largely related to the data sets used to train artificial intelligence systems [53].

As a result of research on biases caused by facial recognition models, systems have evolved and interracial accuracy performances have come close to each other [54]. Research shows the importance of training models with balanced data sets in these improvements [55]. Although we use trained CNN models, these standards are also important for determining appropriate threshold values. Possible performance differences resulting from the use of a fixed threshold value can also lead to bias and negative consequences for disadvantaged groups.

Since we did not want the face recognition models, we used in our study to cause such bias, when calculating the threshold values, we used two separate data sets, one with a balanced diversity of race and gender and the other consisting solely of Black female celebrities. We found that the VGG Face facial recognition model performed over 96% accuracy in both data sets (Mixed Accuracy = 99.82%, BF Accuracy = 96.80%) (Sigma = 2) (Table 3, 4). We found that the FaceNet facial recognition model performed over 99% accuracy in both data sets (Mixed Accuracy = 100.0%, BF Accuracy = 99.37%) (Sigma = 2) (Table 7, 8). In our analysis, we used distance values of the same individuals' images with each other as dependent variables and found that there was no statistically significant difference between the groups (Table 2, 6). However, when we used the appropriate threshold values that we identified (VGG Face and cosine similarity = 0.383, FaceNet and Euclidean l2 = 1.16) we found that both models performed poorly in the Black women data set (Table 4,8). When adjusting the threshold values of models, we used human accuracy performance, measured in the LWF dataset, as a criterion. Since the LWF dataset includes gender and racial diversity, we were able to compare the accuracy performance with the mixed dataset unlike the Black women dataset.

However, at this stage, we think that the threshold value equivalent to 97.5% accuracy performance can be used in the Black women dataset as the threshold value in disadvantaged groups to avoid a bias that can cause by the performance of facial recognition models. As a result of our calculations for this purpose, we found that the VGG Face model works with 97.5% accuracy performance at a threshold of 0.278 in the Black women data set, but is statistically low in reliability (sigma < 2). We found that the FaceNet model works with 97.6% accuracy performance at a threshold of 0.955 on the Black woman data set and has high statistical reliability (sigma > 2). As a result, we have concluded that the threshold value of 0.955, which we calculated with the FaceNet model and Euclidean l2 metric, can be used in disadvantaged groups to avoid a bias caused by the performance of facial recognition models. However, we still think that setting a different threshold range for each group will minimize this potential risk to avoid a possible bias caused by the performance differences of face recognition models.

6.1.2. **Image quality-based challenges.** We know that facial recognition models need to be trained with balanced data sets in terms of gender and race so as not to cause bias. At the same time, factors such as the quality of facial images, and shadow and light ratio directly affect the results produced by face recognition models [50]. Although we use trained CNN models, these standards are also important for determining appropriate threshold values.

When preparing the dataset we used in our study, we made sure that the images had similar quality and light intensity. Nevertheless, we should say that the threshold values obtained in our study are largely valid in the conditions in the data sets prepared by us. However, when we set the threshold values at a high confidence level (sigma = 3), we found that both models produced results close to the original accuracy performance achieved in the LFW dataset, so we think the results can be generalized (For an argument that the LWF dataset does not represent a balanced sample, see [56]).

In order to achieve more reliable results, the data set should be created using photos that have standard qualities. The face recognition model and metric to be used afterward should be determined and a sample set of images should be prepared from the images in this data set and the appropriate threshold value should be determined with the method we described. Similarity calculations should be made with computers with equivalent system performance. Finally, we think that these statistically determined threshold values should be supported by experimental studies in order to be used in real life.

6.2. **Upper Threshold Value.** The fillers selected with the resemble-suspect approach must be within the acceptable similarity range [21]. Therefore, in addition to the lower threshold value that we have set as a stopping point, an upper threshold value should be determined. The upper threshold value is important to prevent the suspect from standing out in the lineup. However, since we can't determine how different the results above the threshold we have determined as a stopping point differ by statistical method, we think that the upper threshold value should be determined via experimental studies. In this respect, we think it is more accurate to select the people closest to the lower threshold (stopping point) as fillers when searching a database until a scientific threshold value is determined.

7. CONCLUSIONS

AI-based systems can be used to control the system variables under the control of the justice system and ensure equal and objective distribution of justice. At the same time, using these technologies in areas that directly affect convictions, such as the legality and reliability of evidence, seems important for the justice system to free

itself from prejudices and improve. Of course, this is only possible provided that the artificial intelligence systems to be used comply with ethical requirements such as the "European Ethical Charter on the use of artificial intelligence (AI) in judicial systems [57]" and legal regulations such as "the Artificial Intelligence Act [58]".

A great deal of research examining wrongful conviction cases reveals that the problem was largely due to misidentification [1-3]. In our study, we focused on the lineup structure, which is one of the factors that cause misidentification, and the approaches used in the selection of fillers to be included in the lineup. The results of the research conducted by Bergold and Heaton showed that fillers selected from large databases with face recognition software bore a lot of similarity to the suspect, which reduced their identification rates [28]. These results have raised concerns that using the suspect resemblance approach in this way, which has yet to have an objective stopping point, will become an increasingly common problem. [13].

In our research, we first focused on detecting an objective stopping point that could be used in the suspect-filler similarity. Using two different facial recognition models with a CNN (Convolutional Neural Network) structure, we calculated optimal threshold values close to human performance (VGG Face and cosine similarity = 0.383, FaceNet and Euclidean l2 = 1.16). To avoid a possible bias caused by the interracial performance of facial recognition models, we have identified a safe threshold value that can be used in disadvantaged groups (FaceNet and Euclidean l2 = 0.955).

However, in order to reach the most reliable threshold values, we have concluded that the face images database to be selected for fillers must be created from images with standard attributes, and that the appropriate threshold value should be determined using the method described in a sample created from face images in this database, and that these statistically determined threshold values should be supported by experimental studies in order to be used in real life.

In the second part of our research, we conducted a study on the problems that are likely to arise from the use of facial recognition software without stopping. With the Betaface (demo) software used by Bergold and Heaton (2018) in their research, we have listed the 10 celebrities who most resembled the corresponding author of this article from the celebrities' database. We found that 8 out of 10 of these people fell below the threshold values we set in both models, which means that these people are too similar to be a filler. The results of the study supported concerns raised by Wells et al. (2020) that facial recognition software would choose fillers that looked too similar to the suspect if they did not have a stopping point.

The results of our study also reveal that models responsible only for facial recognition may not be sufficient in the selection of fillers. Therefore, we concluded that an advanced structure using CNN models trained to recognize other

characteristics (race, gender, age [59]) associated with similarity along with facial recognition models would generate more accurate results.

Author Contribution Statements All authors provided critical feedback and helped shape the research, analysis and manuscript.

Declaration of Competing Interests The authors have no conflict of interest to declare.

REFERENCES

[1] Connor, E., Lundregan, T., Miller, N., McEwan, T., Convicted by Juries, Exonerated by Science: Case Studies in the Use of DNA Evidence to Establish Innocence After Trial, Office of Justice Programs, 1996.

[2] Garrett, B., Convicting the Innocent: Where Criminal Prosecutions Go Wrong, Harvard University Press, 2011.

[3] Innocence Project, Eyewitness Identification Reform, 2018. Retrieved February 17, 2022, https://innocenceproject.org/eyewitness-identification-reform/.

[4] Saks, M. J., Koehler, J. J., The coming paradigm shift in forensic identification science, *Science*, 309 (5736) (2005), 892–895, https://doi.org/10.1126/science.1111565.

[5] Berkowitz, S. R., Loftus, E., Misinformation in the courtroom, H. Otgaar, M. L. Howe (Eds.), Finding the Truth in the Courtroom: Dealing with Deception, Lies, and Memories, Oxford University Press, 2018, 11–20.

[6] Wells, G. L., Applied eyewitness-testimony research: system variables and estimator variables, *J. Pers. Soc. Psychol.*, 36 (12) (1978), 1546-1557, https://doi.org/10.1037/0022-3514.36.12.1546.

[7] Meissner, C. A., Sporer, S. L., Schooler, J. W., Person descriptions as eyewitness evidence, In book: Handbook of Eyewitness Psychology: Memory for People, 2007, 3-34.

[8] Reisberg, D., Heuer, F., Remembering emotional events, Memory and Emotion, Oxford University Press, 2004, 3-41.

[9] Semmler, C., Dunn, J., Wixted, J. T., The role of estimator variables in eyewitness identification, *J. Exp. Psychol. Appl.*, 24 (3) (2018), 400-415, https://doi.org/10.1037/xap0000157.

[10] Siegel, J. M., Loftus, E. F., Impact of anxiety and life stress upon eyewitness testimony, *Bull. Psychon. Soc.*, (12) (1978), 479-480.

[11] Yarmey, A. D., Jacob, J., Porter, A., Person recall in field settings, *J. Appl. Soc. Psychol.*, 32 (11) (2002), 2354-2367, https://doi.org/10.1111/j.1559-1816.2002.tb01866.x.

[12] Wells, G. L., Olson, E. A. Eyewitness testimony, *Annu. Rev. Psychol.,* (54) (2003), 277-

295, https://doi.org/10.1146/annurev.psych.54.101601.145028.

[13] Wells, G. L., Kovera, M. B., Douglass, A. B., Brewer, N., Meissner, C. A., Wixted, J. T., Policy and procedure recommendations for the collection and preservation of eyewitness identification evidence, *Law Hum. Behav.*, 44 (1) (2020), 3-36, https://doi.org/10.1037/lhb0000359.

[14] Wells, G. L., Loftus, E., Eyewitness memory for people and events, Handbook of Psychology: Forensic Psychology, Vol. 11, John Wiley and Sons Inc, 2003, 149-160.

[15] Memmon, A., Higham, P. A., A review of the cognitive interview, *Psychol. Crime Law,* 5 (1-2) (1999), 177-196, https://doi.org/10.1080/10683169908415000.

[16] Semmler, C., Brewer, N., Wells, G. L., Effects of postidentification feedback on eyewitness identification and nonidentification confidence, *J. Appl. Psychol.*, 89 (2) (2004), 334-346, https://doi.org/10.1037/0021-9010.89.2.334.

[17] Davis, D., Elizabeth, L. F., Internal and external sources of misinformation in adult witness, The Handbook of Eyewitness Psychology, Vol. 1. Memory for Events*,* 2007, 195-237.

[18] Wells, G. L., Eyewitness identification: A System Handbook, Carswell Legal Publications, 1988.

[19] Fitzgerald, R., Price, H. L., Valentine, T., Eyewitness identification: Live, photo, and video lineups, *Psychol. Public Policy Law,* 24 (3) (2018), 307-325, http://doi.org/10.1037/law0000164.

[20] Wells, G. L., Steblay, N. K., Dysart, J. E., A Test of the Simultaneous vs. Sequential Lineup Methods an Initial Report of the AJS National Eyewitness Identification Field Studies, 2011.

[21] Luus, C. A. E., Wells, G. L., Eyewitness identification and the selection of distracters for lineups, *Law Hum. Behav.,* 15 (1991), 43-47, https://doi.org/10.1007/BF01044829.

[22] Wells, G. L., Small, M., Penrod, S., Malpass, R. S., Fulero, S. M., Brimacombe, C.A.E., Eyewitness identification procedures: Recommendations for lineups and photospreads, *Law Hum. Behav.*, 22 (6) (1998), 603-647, http://doi.org/10.1023/A:1025750605807.

[23] Fitzgerald, R. J., Oriet, C., Price, H. L., Suspect filler similarity in eyewitness lineups: A literature review and a novel methodology, *Law Hum. Behav.,* 39 (2015), 62-74, http://doi.org/10.1037/lhb0000095.

[24] Fitzgerald, R. J., Price, H. L., Oriet, C., Charman, S. D., The effect of suspect-filler similarity on eyewitness identification decisions: A meta-analysis, *Psychol. Public Policy Law*, 19 (2) (2013), 151–164, https://doi.org/10.1037/a0030618.

[25] Fitzgerald, R., Rubinova, E., Juncu, S., Eyewitness identification around the world, Methods, Measures, and Theories in Eyewitness Identification Tasks*,* 2021, 294-322, http://doi.org/10.4324/9781003138105-16.

[26] Carlson, C. A., Jones, A. R., Whittington, J. E., Lockamyeir, R. F., Carlson, M. A., Wooten, A. R., Lineup fairness: propitious heterogeneity and the diagnostic feature-

detection hypothesis, *Cogn. Res. Princ. Implic.*, 4 (2019), 20–26. http://doi.org/10.1186/s41235-019-0172-5.

[27] Yates, S. Q., Memorandum for Heads of Department Law Enforcement Components All Department Prosecutors, Department of Justice, 2017.

[28] Bergold, N. A., Heaton, P., Does filler database size influence identification accuracy?, *Law Hum. Behav.*, 42 (3) (2018), 227–243, https://doi.org/10.1037/lhb0000289.

[29] National Research Council, Identifying the Culprit: Assessing Eyewitness İdentification, The National Academies Press, 2014.

[30] Police Executive Research Forum (PERF), Library of Congress, 2013. Retrieved December 23, 2021, https://www.loc.gov/item/lcwaN0009235/.

[31] Memon, A., Havard, C., Clifford, B., Gabbert, F., Watt, M., A field evaluation of the VIPER system: A new technique for eliciting eyewitness identification evidence, *Psychol. Crime Law*, 17(8) (2011), 711-729, https://doi.org/10.1080/10683160903524333.

[32] Tredoux, C., A direct measure of facial similarity and its relation to human similarity perceptions, *J. Exp. Psychol. Appl.*, 8 (3) (2002), 180-193, https://doi.org/10.1037/1076-898X.8.3.180.

[33] Valentine, T., A unified account of the effects of distinctiveness, inversion, and race in face recognition, *Q. J. Exp. Psychol. A.,* 43 (1991), 161-204, https://doi.org/10.1080/14640749108400966.

[34] Lee, J., Mansour, J., Penrod, S., Validity of mock-witness measures for assessing lineup fairness, *Psychol. Crime Law*, 28 (3) (2021), 215-245, https://doi.org/10.1080/1068316X.2021.1905811.

[35] Yassin, K., Jridi, M., Falou, A. A., Atri, M., Face recognition systems: a survey, *Sensors*, 20 (2) (2020), 342, https://doi.org/10.3390/s20020342.

[36] Kumar, A., Kaur, A., Kumar, M., Face detection techniques: a review, *Artif. Intell. Rev.,* 52 (2019), 927-948, https://doi.org/10.1007/s10462-018-9650-2.

[37] Manjunath, B. S., Chellappa, R., von der Malsburg, C., A feature based approach to face recognition, *Proceedings 1992 IEEE Computer Society Conference on Computer Vision and Pattern Recognition*, (1992), 373-378, https://doi.org/10.1109/CVPR.1992.223162.

[38] Kalocsai, P., von der Malsburg, C., Horn, J., Face recognition by statistical analysis of feature detectors. *Image Vis. Comput.*, 18 (4) (2000), 273-278, https://doi.org/10.1016/S0262-8856(99)00051-7.

[39] Alzubaidi, L., Zhang, J., Humaidi, A. J., Review of deep learning: concepts, CNN architectures, challenges, applications, future directions, *J. Big Data*, 8 (53) (2021), https://doi.org/10.1186/s40537-021-00444-8.

[40] Serengil, S. İ., Özpınar, A., LightFace: A hybrid deep face recognition framework, *2020 Innovations in Intelligent Systems and Applications Conference (ASYU)*, (2020), 23-27, https://doi.org/10.1109/ASYU50717.2020.9259802.

[41] Yamashita, R., Nishio, M., Do, R.K.G., Convolutional neural networks: an overview and application in radiology, *Insights. Imaging.,* 9 (2018), 611-629, https://doi.org/10.1007/s13244-018-0639-9.

[42] Buolamwini, J., Gender Shades [Master Thesis, Massachusetts Institute of Technology], MIT Media Lab, 2017, https://www.media.mit.edu/publications/full-gender-shades-thesis-17/.

[43] Taigman, Y., Yang, M., Ranzato, M., Wolf, L., DeepFace: Closing the gap to human-level performance in face verification, *Proceedings of the IEEE Computer Society Conference on Computer Vision and Pattern Recognition,* (2014), 1701-1708. https://doi.org/10.1109/CVPR.2014.220.

[44] Serengil, S. İ., deepface/README.md at master · serengil/deepface · GitHub, 2020. Retrieved November 13, 2021, https://github.com/serengil/deepface/blob/master/README.md.

[45] Huang, G. B., Ramesh, M., Berg, T., Learned-Miller, E., Labeled Faces in the Wild: A Database for Studying Face Recognition in Unconstrained Environments, 2007.

[46] Parkhi, O. M., Vedaldi, A., Zisserman, A. Deep Face Recognition, Oxford Robotics Institute, 2015. Retrieved November 23, 2021, https://www.robots.ox.ac.uk/~vgg/publications/2015/Parkhi15/parkhi15.pdf.

[47] Kumar, N., Berg, A., Belhumeur, A., Nayar, S., Attribute and simile classifiers for face verification, *Proceedings of the IEEE International Conference on Computer Vision*, (2009), 365-372, https://doi.org/10.1109/ICCV.2009.5459250.

[48] Schroff, F., Kalenichenko, D., Philbin, J., FaceNet: A unified embedding for face recognition and clustering, *2015 IEEE Conference on Computer Vision and Pattern Recognition (CVPR)*, (2015), 815-823, https://doi.org/10.1109/CVPR.2015.7298682.

[49] Serengil, S. İ., deepface/Fine-Tuning-Threshold.ipynb at master · serengil/deepface. GitHub, 2020. Retrieved November 13, 2021, https://github.com/serengil/deepface/blob/master/tests/Fine-Tuning-Threshold.ipynb.

[50] Krishnapriya, S., Kushal, V., Michael, K., Vítor, A., Kevin, B., Characterizing the variability in face recognition accuracy relative to rac, (2019), arXiv:1904.07325, https://arxiv.org/abs/1904.07325.

[51] Tabachnick, B. G., Fidell, L. S., Using Multivariate Statistics (6th ed.), Boston, MA: Pearson, 2013.

[52] Betaface, Betaface free online demo - Face recognition, Face search, Face analysis, Betaface API. Retrieved February 7, 2022, https://www.betafaceapi.com/demo.html.

[53] Buolamwini, J., Gebru, T., Gender shades: Intersectional accuracy disparities in commercial gender classification, *Proceedings of the 1st Conference on Fairness, Accountability and Transparency, in Proceedings of Machine Learning Research*, 81 (2018), 77-91, https://proceedings.mlr.press/v81/buolamwini18a.html.

[54] Raji, I., Buolamwini, J., Actionable auditing: investigating the impact of publicly

naming biased performance results of commercial AI products, *Conference on Artificial Intelligence, Ethics, and Society,* (2019), https://dam-prod.media.mit.edu/x/2019/01/24/AIES-19_paper_223.pdf.

[55] Tian, J., Hailun, X. A., Hu, S., Liu, J., Multidimensional face representation in a deep convolutional neural network reveals the mechanism underlying AI racism, *Frontiers,* 2021. Retrieved December 26, 2021, https://www.frontiersin.org/articles/10.3389/fncom.2021.620281/full.

[56] Han, H., Jain, A. K., Age, gender and race estimation from unconstrained face images (Rep.), Michigan State University, 2014.

[57] CEPEJ (European Commission for the Efficiency of Justice), European Ethical Charter on the use of artificial intelligence (AI) in judicial systems and their environment, *Council of Europe*, 2018. Retrieved November 11, 2021, https://www.coe.int/en/web/cepej/cepej-european-ethical-charter-on-the-use-of-artificial-intelligence-ai-in-judicial-systems-and-their-environment.

[58] European Commission, EUR-Lex. Retrieved November 11, 2021, https://eur-lex.europa.eu/resource.html?uri=cellar:e0649735-a372-11eb-9585-01aa75ed71a1.0001.02/DOC_1&format=PDF.

[59] Serengil, S. İ., Özpınar, A., HyperExtended LightFace: A facial attribute analysis framework, *2021 International Conference on Engineering and Emerging Technologies (ICEET)*, (2021),1-4, https://doi.org/10.1109/ICEET53442.2021.9659697.

INSTRUCTIONS TO CONTRIBUTORS

Communications Faculty of Sciences University of Ankara Series A2-A3: Physical Sciences and Engineering is a single-blind peer reviewed open access journal which has been published since 1948 by Ankara University, accepts original research articles written in English in the fields of Physics, Engineering Physics, Electronics/Computer Engineering, Astronomy and Geophysics. Review articles written by eminent scientists can also be invited by the Editor.

Article-processing charges: The publication costs for Communications Faculty of Sciences University of Ankara Series A2-A3: Physical Sciences and Engineering are covered by the journal, so authors do not need to pay an article-processing and submission charges. The PDF copies of accepted papers are free of charges and can be downloaded from the webside. Hard copies of the paper, if required, are due to be charged for the amount of which is determined by the administration each year.

Submission: All manuscripts should be submitted via our online submission: https://dergipark.org.tr/en/journal/2457/submission/step/manuscript/new Note that only two submissions per author per year will be considered. Once a paper is submitted to our journal, all co-authors need to wait 6 months from the submission date before submitting another paper.

Cover Letter: Manuscripts should be submitted in the PDF form used in the peer-review process together with THE COVER LETTER and the source file (Supporting File). In the cover letter the authors should suggest the most appropriate Area Editor for the manuscript and potential four reviewers with full names, universities and institutional email addresses. Proposed reviewers must be experienced researchers in your area of research and at least two of them should be from different countries. In addition, proposed reviewers must not be co-auhors, advisors, students, etc. of the authors. In the cover letter, the author may enter the name of anyone who he/she would prefer not to review the manuscript, with detailed explanation of the reason. Note that the editorial office may not use these nominations, but this may help to speed up the selection of appropriate reviewers.

Preparing your manuscript: Manuscripts should be typeset using as DOC or LaTex. Authors will submit their manuscript and the cover letter via our submission system. A template of manuscript can be reviewed in https://dergipark.org.tr/tr/download/journal-file/20554 (or can be reviewed in pdf form).

Title Page: The title page should contain the title of the paper, full names of the authors, affiliations addresses and e-mail addresses of all authors. Authors are also required to submit their Open Researcher and Contributor ID (ORCID)'s which can be obtained from http://orcid.org as their URL address in the format http://orcid.org/xxxx-xxxx-xxxx-xxxx. Please indicate the corresponding author.

Abstract and Keywords: The abstract should state briefly the purpose of the research. The length of the Abstract should be between 50 to 5000 characters. At least 3 keywords are required.

Math Formulae: Formulas should be numbered consecutively in the parentheses ( ).

Tables: All tables must have numbers (TABLE 1) consecutively in accordance with their appearance in the text and a legend above the table. Please submit tables as editable text not as images.

Figures: All figures must have numbers (FIGURE 1) consecutively in accordance with their appearance in the text and a caption (not on the figure itself) below the figure. Please submit figures as EPS, PDF, TIFF or JPEG format.

Authors Contribution Statement, Declaration of Competing Interests and Acknowledgements should be given at the end of the article before the references.

References: The following format for the references should be used. Authors are urged to use the Communication.csl style (https://dergipark.org.tr/en/download/journal-file/18514) in Mendeley Desktop or Zotero automated bibliography. If manual entry is prefered for bibliography, then all citations must be listed in the references part and vice versa. Below, It has no relationship with the text, but can be used to show sample citations such as; for articles [1, 4], for books/booklets/theses [3], and for proceedings/conferences etc. [2].

[1] Demirci, E., Unal, A., Özalp, N., A fractional order SEIR model with density dependent death rate, Hacettepe J. Math. Stat., 40 (2) (2011), 287–295.

[2] Gairola, A. R., Deepmala, Mishra, L. N., Rate of approximation by finite iterates of q-Durrmeyer operators, Proc. Natl. Acad. Sci. India Sect. A Phys. Sci., 86 (2) (2016), 229–234.

[3] Lehmann, E. L., Casella, G., Theory of Point Estimation, Springer, New York, 2003.

[4] Özalp, N., Demirci, E., A fractional order SEIR model with vertical transmission, Math. Comput. Model., 54 (1-2) (2011), 1–6, https://dx.doi.org/10.1016/j.mcm.2010.12.051.

Peer-review policy: The Editor may seek the advice of two, or three referees, depending on the response of the referees, chosen in consultation with appropriate members of the Editorial Board, from among experts in the field of specialization of the paper. The reviewing process is conducted in strict confidence and the identity of a referee is not disclosed to the authors at any point since we use a single-blind peer review process.

Declarations/Ethics With the submission of the manuscript authors declare that:

- All authors of the submitted research paper have directly participated in the planning, execution, or analysis of study;
- All authors of the paper have read and approved the final version submitted;
- The contents of the manuscript have not been submitted, copyrighted or published elsewhere and the visual-graphical materials such as photograph, drawing, picture, and document within the article do not have any copyright issue;
- The contents of the manuscript will not be copyrighted, submitted, or published elsewhere, while acceptance by the Journal is under consideration.
- The article is clean in terms of 'plagiarism', and the legal and ethical responsibility of the article belong to the author(s). Author(s) also accept that the manuscript may go through plagiarism check using IThenticate software;
- The objectivity and transparency in research, and the principles of ethical and professional conduct have been followed. Authors have also declared that they have no potential conflict of interest (financial or non-financial), and their research does not involve any human participants and/or animals.

Archiving: Research papers published in Communications Faculty of Sciences University of Ankara are archived in the Library of Ankara University (Volume 1-63) and Dergipark immediately following publication with no embargo.

Research Articles